DISSERTATIONES
SCIENTIAE
MATERIALIS
UNIVERSITATIS
TARTUENSIS
37

HELLE-MAI PIIRSOO

Mechanical properties of nanocomposites with artificial periodic structure

DISSERTATIONES SCIENTIAE MATERIALIS UNIVERSITATIS TARTUENSIS
37

HELLE-MAI PIIRSOO

Mechanical properties of nanocomposites with artificial periodic structure

UNIVERSITY OF TARTU
Press
1632

Institute of Physics, Faculty of Science and Technology, University of Tartu.

The Dissertation was admitted on June 7, 2024, in partial fulfilment of the requirements for the degree of Doctor of Philosophy in Material Science and allowed for defence by the Scientific Council on Material Science of the Faculty of Science and Technology, University of Tartu.

Supervisors: dr. Aile Tamm, Associate Professor in Materials Science, Institute of Physics, University of Tartu; Head of Research Infrastructures, Ministry of Education and Research, Estonia

dr. Taivo Jõgiaas, Research Fellow in Materials Science, Institute of Physics, University of Tartu

prof. Kaupo Kukli, Professor in Materials Science, Insitute of Physics, University of Tartu

Oponents: dr. Ivo Utke, Team Leader, Department of Advanced Materials and Surfaces, Swiss Federal Laboratories for Materials Science and Technology

dr. Nicolae Spalatu, Senior Researcher, Department of Materials and Environmental Technology, Tallinn University of Technology

Commencement: August 29, 2024, at the University of Tartu, Tartu, Estonia

This work has been partially funded by the European Regional Development Fund project “Emerging orders in quantum and nanomaterials” (TK134) and Estonian Research Agency (PRG4 and PRG753). This work was partially supported by the ERDF project “Center of nanomaterials technologies and research” (NAMUR+, Project No. 2014–2020.4.01.16-0123).

European Union
European Regional
Development Fund

Investing
in your future

ISSN 2228-0928 (print)
ISBN 978-9916-27-592-4 (print)
ISSN 2806-2574 (pdf)
ISBN 978-9916-27-593-1 (pdf)

University of Tartu Press
www.tyk.ee

CONTENTS

PUBLICATIONS INCLUDED IN THE THESIS

I **Helle-Mai Piirsoo**, Taivo Jõgiaas, Peeter Ritslaid, Kaupo Kukli, Aile Tamm. Influence to Hardness of Alternating Sequence of Atomic Layer Deposited Harder Alumina and Softer Tantala Nanolaminates, *Coatings* 12, 404 (2022).
Author's contribution: Preparation of the samples by atomic layer deposition. Characterization of samples with scanning probe microscopy, scanning electron microscopy, and nanoindentation. Preparation of the original draft.

II **Helle-Mai Piirsoo**, Taivo Jõgiaas, Hugo Mändar, Peeter Ritslaid, Kaupo Kukli, Aile Tamm. Microstructure and mechanical properties of atomic layer deposited alumina doped zirconia. *AIP Advances* 11, 055316 (2021).
Author's contribution: Characterization of samples with scanning probe microscopy, scanning electron microscopy, and nanoindentation. Partial analyzation of the extensive X-ray diffraction measurements. Preparation of the original draft.

III **Helle-Mai Piirsoo**, Taivo Jõgiaas, Kaupo Kukli, Aile Tamm. Influence of Annealing on Mechanical Behavior of Alumina-Tantala Nanolaminates. *Materials* 16, 3207 (2023).
Author's contribution: Preparation of the samples by atomic layer deposition and post-deposition annealing. Characterization of samples with scanning probe microscopy, scanning electron microscopy, and nanoindentation. Preparation of the original draft.

IV Aile Tamm, **Helle-Mai Piirsoo**, Taivo Jõgiaas, Aivar Tarre, Joosep Link, Raivo Stern, Kaupo Kukli. Mechanical and Magnetic Properties of Double Layered Nanostructures of Tin and Zirconium Oxides Grown by Atomic Layer Deposition. *Nanomaterials* 11, 1633 (2021).
Author's contribution: Characterization of samples with scanning probe microscopy, scanning electron microscopy, and nanoindentation. Preparation of the figures and text regarding mechanical analysis in the original draft.

V Aile Tamm, Tauno Kahro, **Helle-Mai Piirsoo**, Taivo Jõgiaas. Atomic-Layer-Deposition-Made Very Thin Layer of Al_2O_3, Improves the Young's Modulus of Graphene. *Appl. Sci.* 12, 2491 (2022).
Author's contribution: Characterization of samples with scanning probe microscopy, scanning electron microscopy, and nanoindentation. Preparation of the figures and text regarding mechanical analysis in the original draft.

ABBREVIATIONS

α_i	incidence angle
2θ	diffraction angle
ALD	atomic layer deposition
CSM	continuous stiffness measurement
CVD	chemical vapour deposition
EDX	energy dispersive X-ray spectroscopy
(GI)XRD	(grazing incidence) X-ray diffraction
MEMS	microelectromechanical systems
SEM	scanning electron microscopy
SPM	scanning probe microscopy
STEM	scanning transmission electron microscopy
(WD)XRF	(wavelength dispersive) X-ray fluorescence spectroscopy
XRR	X-ray reflectivity

THE CLAIM OF THE THESIS

The mechanical properties, i.e. hardness and, complementarily, elasticity, of atomic layer deposited metal oxide thin films grown to thickness markedly below 100 nm, can be modified in a controllable manner. Notably, the mechanical hardness can be engineered to gradually increase or decrease throughout the depth of the thin oxide film.

The mechanical behaviour of coatings in nanoscale thickness can controllably be modified by adding constituents to the host material that can: (i) reinforce the softer functional material by restricting its deformation; (ii) induce crystallization, phase transformation, and/or preferred orientation during deposition; (iii) induce crystallization, phase transformation, and/or preferred orientation during post-deposition annealing; (iv) influence the residual stresses in the film.

1. INTRODUCTION

1.1 Prospective applications of solid, hard, and functional thin films

Metal oxide thin films are functional components in nanodevices such as micro-electromechanical systems (MEMS), memristors, transistors, capacitors.

Amorphous 5 nm thick Al_2O_3/Ta_2O_5 bilayer is applicable as the resistive switching medium in an analogue memristor device [1]. The thickness ratio of Al_2O_3 and Ta_2O_5 layers in a thin multi-layered film may allow one to modify the operating range and mechanisms of high voltage capacitor devices [2]. The highest dielectric strength has been achieved with exactly two Al_2O_3/Ta_2O_5 bilayers [3]. Breakdown voltages and currents of the Al_2O_3/Ta_2O_5 nanocomposite thin films depend on the number of layers as well [3].

Tetragonal/cubic ZrO_2 thin films can possess high dielectric strength which makes them useful in capacitor devices [4–5]. Al_2O_3, alternately layered with ZrO_2, helps to stabilize the tetragonal/cubic phases and reduce leakage currents [4–6]. Al_2O_3/ZrO_2 multilayers were found suitable for memristors as well [7].

However, if a functional thin film is prone to mechanical failure, any (including electrical) device can remain fragile, and may not function properly. Microscale springs, beams, membranes, gears are structural components in micro-gas turbines, micro-engines, pressure sensors, accelerometers, microswitches, micromirrors [8–9]. The materials in these MEMS need to resist cyclic loads, bending, or wear while retaining their functional properties such as electrical insulation, ferromagnetism, or optical transparency. The main reason for MEMS failure is wear [8–9]. Therefore, the mechanical properties of metal oxide thin films are of interest as they affect the reliability of nanodevices.

1.2 Achievements published to date

There are a few studies on the mechanical properties of composite thin films made by atomic layer deposition (ALD) published so far [10–20]. A detailed overview of the mechanical characterization of ALD nanocomposites is presented in Chapter 3.2. The properties of any composite depend on the intrinsic properties of its constituent materials, such as metal oxides. However, it is possible to create composite materials which are harder than its constituent pure oxides [20]. Often, the influence on the mechanical properties can be explained by the changes in the crystal structure of the material caused by doping or periodic layering. Layering can significantly reduce residual stresses [13–14]. A couple of studies have also noted the possibility that the deposition sequence of constituent layers can affect the mechanical properties of the laminate [13, 16].

1.3 Objectives

The aim of this work is to study possible methods to engineer mechanical properties of atomic layer deposited metal oxide thin films. The results will add to the knowledge on how to increase the mechanical reliability of functional thin films or create hard protective thin films for MEMS. The hardness and Young's modulus of the composite thin films were determined by nanoindentation.

2. NANOINDENTATION OF THIN FILMS

This instrumented indentation method implements a diamond probe to apply a load *P* to a sample to initiate, first, elastic deformation, and, then additionally, with increasing stress, plastic deformation. The displacement *h* of the probe from the initial surface level into the sample due to the deformation is registered. A typical load – displacement *P-h* curve is depicted in Figure 1. Several parameters of that curve allow to determine the elastic (Young's) modulus *E* and hardness *H* of the material [21].

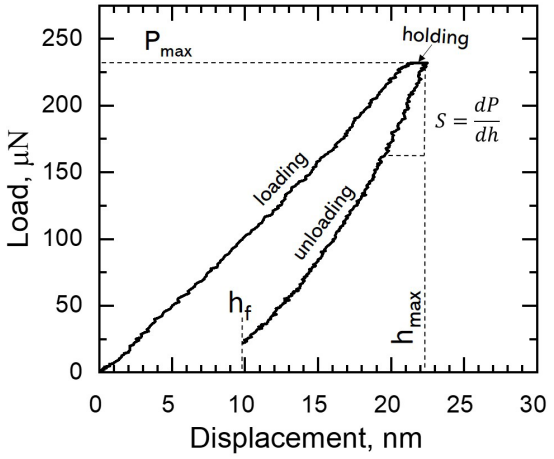

Figure 1. Load – displacement curve of a quasistatic nanoindentation test, where P_{max} is the maximum load applied by the probe, h_f is the final depth of the indent, h_{max} is the maximum displacement achieved by the probe, and S is the contact stiffness equal to $\boldsymbol{dP/dh_{h=h_{max}}}$.

The hardness of the material is equal to the mean contact pressure, i.e. the ratio of the applied maximum load and projected area of the indent [22]:

$$H = \frac{P_{max}}{A(h)} \tag{1}$$

The determination of the contact area *A* is described in detail in section 2.2. The hardness measured with nanoindentation can vary compared to the traditional indentation techniques as the contact area is determined during loading before elastic recovery. The stresses in the sample must be high enough to initiate plastic flow in order to determine hardness at all [21–22].

The unloading part of the *P-h* curve is the result of the elastic recovery after withdrawal of load and can be described with a power law [21, 23]:

$$P(h) = \alpha(h - h_f)^m \tag{2}$$

The exponent m varies between 1.2 and 1.6 for Berkovich tip and constant α is characteristic to the material. The stiffness of the contact S is defined as $dP/dh_{h=h_{max}}$ and is related to the elastic modulus of contact E_c [21]:

$$E_c = \frac{\sqrt{\pi}S}{\beta 2\sqrt{A}} \tag{3}$$

The correction factor β accounts for the errors due to non-axisymmetry of real probes and for Berkovich tip the value 1.05 gives good results [21].
Young's moduli of the sample E_s and the probe E_p, and their Poisson's ratios are related to the contact modulus E_c through given relationship [21]:

$$\frac{1}{E_c} = \frac{1-v_s^2}{E_s} + \frac{1-v_p^2}{E_p} \tag{4}$$

2.1 Hardness and elastic modulus by dynamic nanoindentation

The stiffness can be determined throughout the depth probed by applying load with a superimposed sinusoidal oscillation:

$$P = P_0 e^{i\omega t} \tag{5}$$

This results in an oscillating displacement signal with a slight phase difference due to sample and instrument damping:

$$h = h_0 e^{i(\omega t+\varphi)} \tag{6}$$

The load amplitude P_0, displacement amplitude h_0, and phase φ are measured with a certain frequency in the range from 1 to 300 Hz. Previously determined system parameters like transducer damping coefficient C_T, transducer mass m_T, transducer stiffness k_T and the oscillation frequency ω influence the contact stiffness $k_{storage}$ and the amount of sample damping C_s [24–25]:

$$k_{storage} = \frac{P_0}{h_0} cos\varphi + m_T\omega^2 - k_T \tag{7}$$

$$C_s = \frac{P_0}{h_0}\frac{sin\varphi}{\omega} - C_T \tag{8}$$

Errors from the machine compliance and sample damping can be considered with the complex stiffness:

$$k_{complex} = \frac{1}{\frac{1}{\sqrt{k_{storage}^2 \pm (\omega C_s)^2}} - [MC]} \tag{9}$$

Machine compliance can be determined with a calibration procedure, however, it contributes a significant contribution to the measurements only at higher loads (>5 mN) [21]. Sample damping C_s or loss stiffness $k_{loss}=\omega C_s$ describe the creep properties of viscoelastic materials. Storage, loss, and complex moduli of the contact can be determined with equation 3. For fully elastic materials storage and complex moduli coincide [24–25]. Dynamic nanoindentation measurement is called continuous stiffness measurement (CSM) as elastic modulus and hardness can be found from stiffness values determined through the probed thickness.

2.2 Contact area function

The main advantage of nanoindentation before other indentation techniques is the determination of the contact area projection from the load – displacement graph. The contact area function *A(h)* describes the relationship between projection of the contact area between probe and sample (depicted in Figure 2) and the displacement of the probe detected by the transducer. The function depends on the geometry (sphere, cone, pyramid) of the probe. The Berkovich tip, which is common in nanoindentation and also used in this work, is a symmetric three-sided pyramid with a 65.27° face angle (Figure 2). For ideal geometry of the tip the contact area function would be as follows [22]:

$$A = 24.5h_c^2 \tag{10}$$

Contact displacement h_c is less than the maximum probe displacement h_{max} as elastic deformation causes the initial surface around the probe to sink-in (Figure 2). The level of sink-in h_s depends on the applied load, stiffness of the material, and probe geometry. Meaning, the contact displacement can be found with equation [21]:

$$h_c = h_{max} - \frac{0.75P_{max}}{S} \tag{11}$$

The influence from the roundedness of a real tip is considered by performing indentations on a reference sample and fitting the results to a polynomial area function [21]:

$$A = \frac{\pi}{4}\left(\frac{S}{E_c}\right)^2 \tag{12}$$

$$A(h) = C_0h^2 + C_1h + C_2h^{\frac{1}{2}} + C_3h^{\frac{1}{4}} + C_4h^{\frac{1}{8}} + C_5h^{\frac{1}{16}} \quad (13)$$

Stiffness S is measured on fused quarts with contact modulus of 69.6 GPa at various displacements and constants *C0–C5* are found by curve fitting to the results. The accuracy of the contact area function can be enhanced by restricting the fitting displacement range [21].

Plastic flow of sample material around the probe can cause pile-up instead of sink-in, which can cause overestimation of both hardness and Young's modulus by 50% with incorrect contact area [26]. Pile-up depends on the yield strength to elastic modulus ratio and strain hardening behaviour of the material. It has been shown that h_f/h_{max} ratios below 0.7 indicate the absence of pile-up [26]. Otherwise, other methods than given above have to be implemented to determine the correct values for hardness and modulus. Pile-up can be a bit more prevalent in thin-film-substrate systems when the downward plastic flow of the more softer film material is restricted by the substrate [27–28].

In addition to predicting pile-up, the parameter h_f/h_{max} is related to *H/E* ratio that describes the tribological properties of the material. Higher values for *H/E* indicate to higher contact elasticity between surface asperities, while higher values for h_f/h_{max} ratio indicate to higher plasticity [29].

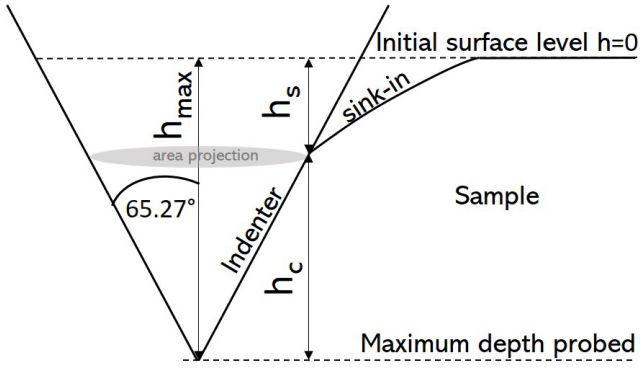

Figure 2. Descriptive cross-section of probe – sample contact under maximum load applied. Maximum, contact, and sink-in displacements are depicted by h_{max}, h_c, and h_s, respectively.

2.3 Hardness of thin-film-substrate composite

Substrate influences nanoindentation measurements of a thin film. This results in measured composite hardness H_c at displacements that exceed a critical fraction of the film thickness. The critical fraction ranges between 0.07 and 0.5, dependent on the difference in the mechanical properties of the substrate and coating [27–28]. One of the models that describes the relationship of composite hardness and displacement was developed by Puchi-Cabrera *et al*. [30]. Composite hardness is dependent on the hardness of the substrate H_s, thickness t_f and hardness of the

film H_f or thickness $t_{f,i}$ and hardness $H_{f,i}$ of individual layers in a multi-layered thin film. The model is based on linear (Voight) law of mixtures:

$$H_C = \sum_{i=1}^{N} a_{f,i} H_{f,i} + a_s H_s \tag{14}$$

For a multi-layered thin film, with N number of layers, the volume fractions a_f affecting H_c at a given displacement can be found:

$$a_{f,j} = 1 - \sum_{i=1}^{j-1} a_{f,i} \qquad \text{if} \qquad h < \sum_{i=1}^{j} K_{f,i} t_{f,i} \tag{15}$$

$$a_{f,j} = exp\left[-\left(\frac{h - \sum_{i=1}^{j} K_{f,i} t_{f,i}}{\beta_j \sum_{i=1}^{j} t_{f,i}} \right)^2 \right] - \sum_{i=1}^{j-1} a_{f,i} \qquad \text{otherwise} \tag{16}$$

Fitting parameters K and β represent, respectively, the critical thickness fraction and displacement-to-thickness ratio when $(H_c\text{-}H_s)/(H_f\text{-}H_s)$ becomes constant with further increase of displacement. The model has been derived for Vickers indenter and analysed for coatings with thicknesses at least several micrometers [30].

2.4 Microscopy of indents

Different microscopy methods can support and supplement the nanoindentation results for films with the lowest thicknesses and even single layers (graphene) [21–22, 31]. Some indentation devices can perform scanning probe microscopy (SPM) with the same Berkovich tip used for indentations. The method allows to select exact surface feature of interest for indentation measurements and to procure an image of the plastic deformation mark after indentation. It is possible to detect pile-up [17] and cracking [**III**] or even establish the minimum load required to initiate plastic flow during indentation. In Figure 3 hardness was calculated from a *P-h* curve, while the indent cannot be discerned from the SPM image with certainty. Therefore, the prompt imaging of the indents after measurement, could be used to detect the minimum load at which point indents are distinguishable and hardness can be determined correctly.

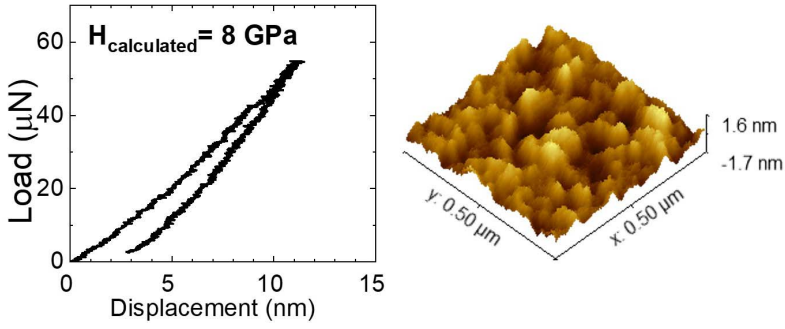

Figure 3. Load-displacement graph of an „indent“ visualized by SPM image on the right. The lateral and vertical scales of the images are not proportionate.

3. MECHANICAL PROPERTIES OF LAYERED THIN FILMS

3.1 Mechanical properties of nanocomposites

Nanocomposite coatings with various nanostructures (heterostructure, multilayer, nanocrystals in amorphous matrix) have been used as super hard protective coatings. The architecture of these nanocomposites has been shown to influence their mechanical properties and not always according to the mixture law of composites [29].

Influence of grain sizes on the strength and hardness is described with Hall-Petch law ($H \sim d^{-1/2}$) for bulk materials as well. However, when grains are about 10 nm in size, the law breaks down as deformation mechanisms change. Additional amorphous monolayer between such nanograins increases the hardness by restricting plastic flow. Ultrahigh hardness (>100 GPa) can be achieved [29].

Heterostructures consist of less than 10 nm thick layers with sharp interfaces that restrict dislocation generation. When the elastic moduli of the layers differ significantly, the glide of dislocations from layer to layer is restricted and the hardness of the coating can exceed 50 GPa [29, 32]. Multilayers with rougher interfaces and thicker layers are more easily manufactured and possess relatively high hardness and toughness, suitable for cutting tool applications [29, 33]. There have been reports indicating the possible improvement of hardness by compressive residual stresses in coatings [33].

3.2 Mechanical properties of ALD nanolaminates

Mechanical properties such as hardness, elastic modulus, residual stresses, and wear resistance of some atomic layer deposited metal oxide composites have been reported earlier [10–20]. Materials under investigation have been, for example, amorphous Al_2O_3, Ta_2O_5, SiO_2 and polycrystalline ZrO_2, ZnO, HfO_2, TiO_2. Constituent oxides have been stacked with variable single layer thicknesses while volume fraction ratio was either varied or held constant**.** Films deposited with the aim to procure bilayer thickness below 0.8 nm have been shown to possess isotropic structure rather than layers [34]. Such composites are commonly referred to as mixtures**.** The total thickness of all of these composite films has varied between 90 and 200 nm.

Several groups have studied amorphous Al_2O_3 and crystalline/amorphous TiO_2 nanolaminates [13–15]. Crystallinity of TiO_2 layer between Al_2O_3 layers is affected by their thicknesses. The laminate is X-ray amorphous if the TiO_2 layer thickness is below 25 nm, while reference TiO_2 film deposited with the same process parameters shows crystallinity [13–15]. The introduction of amorphous Al_2O_3 layers into TiO_2 film reduces residual tensile stresses and the level of reduction depends on the Al_2O_3/TiO_2 layer thickness ratio [13–14]. Optimal stacking configuration was determined to be 7.7 nm of Al_2O_3 and 40 nm of TiO_2

in a 200 nm thick film and the overall tensile stress reduction achieved was 100 MPa [13]. For completely amorphous laminates, however, the tensile stress decreased from 430 ± 70 MPa to 260 ± 60 MPa as bilayer thickness increased from 0.8 nm to 50 nm [14]. In addition, at the deposition temperature of 100 ºC the deposition sequence of oxide layers significantly influenced the residual stress level [13]. In contrast, amorphous SiO_2 in the TiO_2 laminates did not lower the stress at all [13].

Ylivaara *et al.* [14] reported that even as the mechanical stresses changed in amorphous Al_2O_3/TiO_2 laminates, the hardness and modulus did not vary significantly, only changing from 7.8 ± 0.1 GPa to 8.2 ± 0.2 GPa and from 145 ± 1 MPa to 155 ± 1 GPa, respectively. The hardness and modulus were found to decrease with the Al_2O_3 volume fraction, while tensile stresses remained unaffected. Nanoindentation measurements in this study were gathered at displacements of 40 nm [14]. Another study by Coy *et al.* [15] on similar laminates implemented a more surface sensitive indentation – reliable results were gathered at displacements of 20 nm [15]. Modulus reached 162 ± 2 GPa in the case of 10 nm thick bilayers in a 100 nm thick amorphous Al_2O_3/TiO_2 laminate and decreased to a level comparable to values reported by Ylivaara *et al.* [14] at the displacement of 40 nm. Hardness, as reported by Coy *et al.* [15], was ~ 9 GPa for the films with 10 and 2.5 nm thick bilayers. Thicker bilayers resulted in a softer composite. Overall, the hardness of both the laminates and the reference oxide films reported by Coy *et al.* [15] were consistently 1 GPa higher compared to the values shown by Ylivaara *et al.* [14]. Hardness of thin films was shown to be sensitive to any slight changes in process parameters as both publications reported on similar precursors and deposition temperatures in similar reactors [14–15].

Kilpi *et al.* [10] found that the amorphous Al_2O_3/TiO_2 laminates, that were previously characterized by Ylivaara *et al.* [14], caused much less wear on a silicon pin in tribological MEMS tests compared to reference oxide films.

Al_2O_3 interlayer was found to decrease the residual tensile stresses of HfO_2 films as well. Stress was reduced by 200 MPa when 3 nm of amorphous Al_2O_3 was alternated with 7.5 nm of amorphous HfO_2 in a 200 nm thick film [11]. This led to the improvement of the mechanical stability of a dichroic mirror device [11].

An intermediate 10 nm thick amorphous Al_2O_3 layer was added to a crystalline V_2O_5/ZnO composite to induce a preferential crystallographic growth direction for the top ZnO layer [18]. As a result, textured ZnO layer with a lower surface friction coefficient was grown [18]. In addition to texture, layering ZnO with Al_2O_3, allows one to control the size of crystallites [20]. Maximum hardness of 11 GPa, exceeding the hardness of the reference oxide films, was achieved in a laminate with the average crystallite size of 10 nm. Critical crystallite size at which point the Hall-Petch law starts to reverse has been reported to be around 20–5 nm [29, 35]. Volume fraction of Al_2O_3 in the ZnO laminates influenced the mode of the wear deformation as well [20].

Graphene was found to influence the preferential orientation of ZnO as the relative intensity 002 reflection increased with the number of graphene layers in

the film [12]. The crystallite size of ZnO was decreased with each added graphene layer, together with the hardness and modulus of the composites. This was probably due to poor interfacial strength between the materials. Two layers of graphene in a 100 nm thick ZnO film resulted in the material with the highest elastic modulus (200 GPa) and hardness (8 GPa) out of all the studied films [12].

Additional thin amorphous Al_2O_3 layer has induced phase transformation and produced texture in crystalline ZrO_2 [19]. If the layer thickness of ZrO_2 was held constant and volume fraction of Al_2O_3 increased, the laminate, eventually, becomes completely amorphous. There exists a critical ZrO_2 layer thickness for which the additional Al_2O_3 does not impact the shape of the X-ray diffractogram. Neither the layer structure nor phase composition has affected the elastic modulus of such laminates [19]. Their hardness was estimated to rise up to 16 GPa at the surface and seemed somewhat dependent on the layer architecture [19].

In an earlier study, layered architecture of amorphous Al_2O_3/Ta_2O_5 had no effect on the hardness and modulus, measured as high as 7.0 ± 0.5 GPa and 95 ± 5 GPa, respectively [16]. For ZrO_2/amorphous Ta_2O_5 nanolaminates the hardness reached maximum of 7.8 GPa when single oxide layer was 2.5 nm thick, while the elastic modulus (110 GPa) remained unaffected by the layer architecture. In these laminates, ZrO_2 became amorphous when constituent layers were below 5 nm, meaning the laminate that possessed maximum measured hardness was entirely amorphous [16]. Similarly, for crystalline HfO_2/amorphous Ta_2O_5 nanolaminates the hardness reached maximum of 7.4 GPa when single oxide layer was 15 nm thick, while the elastic modulus varied randomly between 95–115 GPa independently from material's structure [16]. HfO_2 became amorphous when constituent layers were below 10 nm, meaning, unlike the ZrO_2/Ta_2O_5 laminate, HfO_2/Ta_2O_5 laminate possessed maximum measured hardness with crystalline HfO_2 layers [16]. In addition, the sequence of the constituent layers in the reported Ta_2O_5 laminates somewhat affected the mechanical properties [16].

Diffractograms of crystalline ZrO_2/HfO_2 laminates depended on the bilayer thickness and the maximum elastic modulus of 105 GPa was achieved in the films grown applying 8 growth cycles per constituting layer, while hardness of 10 GPa remained the same for films grown using 2 and 8 cycles per layer [17].

To conclude, layered architecture, characteristic of nanolaminates, affects the crystallinity of the materials. Preferential orientation, phase composition, and crystallite size in the multilayers can be modified. Layering can reduce residual stresses in thin films and change the deformation modes. However, optimum layer structures resulting in the highest hardness and elastic modulus may not always coincide. Compared to elastic modulus hardness is somewhat more sensitive to any changes in materials' structure.

4. FABRICATION AND STRUCTURAL ANALYSIS OF LAYERED NANOCOMPOSITES

4.1 Atomic layer deposition

Atomic layer deposition allows one to deposit a layer of material with accurately controlled thickness on arbitrarily shaped or structured substrates making the method crucial for the fabrication of MEMS and other nanodevices [36–37]. The coating conformality and control over thickness is achieved through cycled form of deposition with self-terminating surface reaction. Each cycle consists of: (i) precursor A pulse that results in chemisorption of a partial monolayer by self-terminating gas – surface reaction; (ii) purge pulse with inert gas to remove all traces of the precursor A and reaction by-products; (iii) precursor B pulse that results in chemisorption of a secondary partial monolayer; (iv) purge pulse (see Fig. 2 in ref. [36]). The deposition rate is described by the average thickness of the material grown in one cycle – growth per cycle (nm/cycle).

The reactions take place at a finite number of chemically active sites on the substrate surface, which are reactive functional groups like –OH. An abundance of reaction sites can lead to a two-dimensional material growth, while absence of sites, for example on the surface of inert graphene, can lead to nucleation and island growth at defects [36]. The hydrogen-terminated Si(100) surface reduces the growth per cycle of amorphous Al_2O_3 with TMA and H_2O precursors compared to the hydroxyl-terminated Al_2O_3 surface. Atomic layer deposition starting at a new substrate can possess variance in growth per cycle until it stabilizes by the 10^{th} cycle. The substrate can affect the growth mode, growth per cycle and even phase composition of the thin film [37]. For example, Al_2O_3 grows amorphous on most substrates at temperatures lower than 600 ºC, but crystalline growth can be initiated by epitaxy on a suitably crystalline substrate like sapphire, niobium single crystals [38], Cr_2O_5 [39].

In addition to substrate, the selection of precursors, deposition temperature and alloying/doping can influence the phase composition, preferred orientation of crystals, crystal size, and level of impurities left in the film. Even the thickness of the thin film that is controlled by the number of deposition cycles implemented, can have an effect on the structure of the film [37]. The through-thickness stable phase of ZrO_2 film changes from cubic/tetragonal to monoclinic with the increasing thickness [40].

For crystalline growth the grain size can exceed the overall thickness of the films which lead to relatively high surface roughness. Post-deposition annealing can be implemented to crystallize amorphous films, however, the annealing temperature and time needed for phase transformations is dependent on the film thickness [37].

Since atomic layer deposition enables exact control over thickness and produces an uniform thickness conformally, it can be used to deposit nanolaminates with high quality periodicity and sharp interfaces [41–42]. Attention must be paid

on the adhesion, reaction sites, growth per cycle between the surfaces of the constituents [36, 42]. On the other hand, alloying or doping of a film in ALD process will not lead to uniform distribution of alloying/doping element through the thickness [43].

4.2 Grazing incidence X-ray diffraction

The phase composition, crystal structure, lattice parameters, size, shape and preferential orientation of crystallites, internal stresses, and even thickness of thin films can be characterized by grazing incidence X-ray diffraction (GIXRD) [44–45]. X-ray diffraction implements monochromatic (Cu Kα) radiation that interferes constructively after scattering elastically, i.e. diffracting, from periodically spaced atoms when Bragg's law conditions are met. Diffractograms are intensity – diffraction angle 2θ graphs, where signals due to diffraction are called reflections. For thin film measurements incidence angles α_i, between primary beam and sample surface, are kept stationary and below 1° yet above the critical angle of total external reflection α_c. Low incidence angle produces signals with higher intensity from the top layers of the sample as the beam length of the rays increases within these layers, which, in turn, increases the volume of the irradiated material [46]. However, low α_i can also cause the position of a reflection to shift slightly (~0.4 deg) due to refraction [44] and nonsymmetric α_i-2θ scan can cause changes to the relative intensities of reflections when the measured polycrystalline material does not possess random orientation of crystallites [46]. It is possible to estimate the depth of the GIXRD measurement with incidence and critical angles [44, 47–48]:

$$\Lambda = \frac{\lambda}{4\pi} \sqrt{\frac{2}{\sqrt{(\alpha_i^2 - \alpha_c^2)^2 + \frac{\lambda^2\mu^2}{4\pi^2}} - (\alpha_i^2 - \alpha_c^2)}} \tag{17}$$

Penetration depth of X-rays Λ is the distance X-rays pass through in the material until the intensity has reduced by factor of $1/e$. Linear attenuation coefficient μ can be found with atomic absorption coefficients of constituent elements. The critical angle of total reflection of a material can be determined with X-ray reflectivity measurements or calculated with the equation [47–48]:

$$\alpha_c = \sqrt{\frac{r_e N_A \lambda^2}{\pi} \frac{\rho}{M} \sum_Z w_Z (f_{0Z} + \Delta f_Z')} \tag{18}$$

Electron radius r_e, Avogadro's number N_A, wavelength of the diffracting beam λ are constants, while density ρ, molar mass M, element fraction w_Z are dependent on the chemical composition of the material and the atomic scattering factor ($f = f_0 + \Delta f' + i\Delta f''$) is dependent on the element and wavelength. It is possible

to gather information about the crystalline structure of thin films at different depths, i.e. perform depth-profiling, by varying the incidence angle.

Preferential crystallographic orientation of grains means that the material is textured, which can affect the physical properties including mechanical behavior. A highly textured polycrystalline material can resemble monocrystalline material in terms of anisotropy of its properties. Symmetrical XRD measurement can determine the level of texture in a material from the relative intensities of reflections [46]. The non-symmetric grazing incidence method, however, complicates the investigation of texture and can be used to simply detect its presence [46].

5. EXPERIMENTAL GOALS

The aim of the experiments was to investigate possibilities to synthesise thin solid materials with predeterminable mechanical characteristics, i.e. hardness and elasticity. The physical properties of (nano)composites are modifiable by the fraction and choice of constituent materials and the artificial structure of the composite. An artificial periodic nanostructure i.e. nanolaminate, can be deposited by atomic layer deposition as the deposition parameters allow one precise control over the architecture of the thin films. One should, potentially, be able to deposit thin films with various periodic structures over large areas on arbitrarily shaped substrates. In such thin composite films, the mechanical properties are influenced by multiple characteristics: the chemical composition, the phase composition, and the artificial periodic structure. The phase composition, in turn, can be influenced with the artificial structure and the precursor chemistry. In this work, well-established ALD precursor chemistries were used in order to conveniently build the nanolaminates and study the influences from the periodicity. The mechanisms to modify the mechanical properties include reinforcements from the laminate structure and changes in the phase composition due to the artificial periodicity. Internal residual stress distribution in thin films can be modified by the architecture [13–14]. Therefore, a set of amorphous and crystalline metal oxides were deposited by ALD in multiple configurations of artificial periodic structures to study the different mechanisms influencing the hardness and Young's modulus of thin composite films.

Aluminium(III) oxide was deposited with $Al(CH_3)_3$ and water precursors (further details in Chapter 6.1). It is widely studied and implemented ALD process with highly reactive and self-limiting reactions that generate inert residual products with relatively high growth rate (~0.09 nm/cycle) [36]. The Al_2O_3 thin films remain amorphous at annealing temperatures up to 800 ºC [49]. The hardness and the elastic modulus of amorphous Al_2O_3 ALD films is, respectively, 10 ± 2 GPa and 145 ± 20 GPa according to various reports as shown in Table 1. Amorphous Al_2O_3 layers in ALD nanolaminates have shown to influence the crystal structure and mechanical residuals stresses of constituents [11, 13–16, 18–20].

Tantalum pentoxide was deposited with $Ta(OCH_2CH_3)_5$ and water precursors (further details in Chapter 6.1). This is a well-established ALD process that allows one to produce amorphous stoichiometric Ta_2O_5 films with uniform thickness [50]. Growth rate remains around 0.04 nm/cycle [50]. Amorphous Ta_2O_5 films crystallize at annealing temperatures of more than 700 ºC [51–52] and most likely form the orthorhombic Ta_2O_5 phase, instead of the hexagonal one that has coinciding XRD reflections, according to the selective area electron diffraction analysis done by Min *et al*. [53]. The hardness and Young's modulus of amorphous Ta_2O_5 ALD films has been reported to be 6.7 and 96 GPa, respectively, on a glass substrate (Table 1) [16]. The hardness and Young's modulus of ion beam sputtered amorphous Ta_2O_5 films were, respectively, 6.5 and 132 GPa [54]. The

hardness and Young's modulus of magnetron sputtered amorphous Ta_2O_5 films were, respectively, 8.2 and 153 GPa [55]. The hardness and Young's modulus of crystalline Ta_2O_5 films prepared by ion beam sputtering were, respectively, 8.1 and 142 GPa [54] and by magnetron sputtering, respectively, 14.3 and 188 GPa [55].

Zirconium dioxide was deposited with $ZrCl_4$ and water precursors (further details in Chapter 6.1). Again, the process is well-known and used to produce ZrO_2 thin films consisting monoclinic, tetragonal, and cubic phases with relatively high growth rates (~0.1 nm/cycle) [40]. Whereas, the phase composition has been found to be dependent on the deposition temperature and film thickness. Combining ZrO_2 with Al_2O_3 could enable one to stabilize the tetragonal and cubic phases even as the film thickness increases [6], which could potentially allow one to attain ALD thin films with hardness' up to 20 GPa [56–57]. Previously, the hardness and the Young's modulus of ALD monoclinic ZrO_2 films has been 7 and 86 GPa, respectively, on a glass substrate (Table 1) [16].

Tin dioxide was deposited with SnI_4 and O_3 precursors (further details in Chapter 6.1). This process works in a wide temperature range (200–600 ºC) with high growth rate (0.25 nm/cycle) [58]. The mechanical properties of atomic layer deposited SnO_2 has not been reported on previously, however the hardness and elastic modulus of chemical vapour deposited (CVD) F-doped SnO_2 was around 8 and 70 GPa, respectively [59].

Table 1. Hardness and Young's modulus of reference metal oxide ALD thin films as reported in earlier studies and measured in this work.

ALD material	Hardness (GPa) reported	Hardness (GPa) measured	Modulus (GPa) reported	Modulus (GPa) measured
Al_2O_3	8.8 [15] 7.7 [20] 12 [19] 9.5 [16] 9.9 [14]	11.2 [**I**] 11.1 [**II**] 18* [**III**]	143 [15] 135 [20] 150 [19] 68 [16] 156 [14]	154 [**I**] 145 [**II**] 170* [**III**]
Ta_2O_5	6.7 [16]	8.2 [**I**] 12.0* [**III**]	96 [16]	139 [**I**] 155* [**III**]
ZrO_2	7.0 [16]	12.2 [**II**] 11.5 [**IV**]	86 [16]	127 [**II**] 96 [**IV**]
SnO_2	–	14.8 [**IV**]	–	175 [**IV**]

* after annealing

Graphene is known for its good mechanical properties such as high Young's modulus (1000 GPa) and strength (130 GPa) [60]. However, in practice, the grain boundaries developing in the material during fabrication by chemical vapour deposition (CVD) significantly reduce its resistance to deformation and failure [61–62].

Constituent materials were deposited in various configurations. The exact number of deposition cycles with their order is shown in Chapter 6.1.

Bilayers with constituents of equal volume fraction were deposited with amorphous Al_2O_3/Ta_2O_5 and crystalline ZrO_2/SnO_2 with the total film thickness of 75 and 21 nm, respectively. The sequence of constituent layers was alternated. The mechanical properties of the chosen constituent materials varied only slightly. The influence of the architecture of the layers on the hardness and Young's modulus was investigated. The influence from the total film thickness on the mechanical characterization was of interest, i.e. is it possible to attain credible results from such thin layers.

Post-deposition annealing was implemented at 700 and 800 ºC for 10 min in air for the amorphous bilayers to crystallize the Ta_2O_5 layers. Changes to the microstructure of ALD nanolaminates after post-deposition annealing depend on the constituent materials and their layered structure. The crystallization temperature of ZrO_2 layers increased with the decreasing layer thickness when it was alternated with SiO_2 layers [63]. The crystallization temperature of TiO_2 layers, on the contrary, lowered when it was layered with Al_2O_3 compared to the reference pure oxide film [13]. After annealing only the topmost layer of HfO_2 crystallized in La_2O_3/HfO_2 nanolaminates [64]. Hence, the influence from the sequence of layers and their thickness on the phase composition and mechanical properties of the laminates after annealing was studied.

Trilayers of amprhous Al_2O_3/Ta_2O_5 with alternating layer sequence and total thickness of 75 nm were deposited and post-deposition annealing was similarly implemented. The influence of a single layer thickness on the structure and mechanical properties of the film were investigated. Silicon (100) substrate was used for all the afore mentioned layered thin films.

Periodic doping was implemented to attain cubic ZrO_2 thin films. Only a single deposition cycle of Al_2O_3 between multiple cycles of ZrO_2 was done in order to produce uniform crystalline ZrO_2 film. A single deposition cycle does not produce a distinct layer of Al_2O_3, however, a periodic Al_2O_3 concentration distribution through the thickness of the film is developed, instead of an uniform chemical composition [43]. The number of ZrO_2 cycles between Al_2O_3 cycles were increased from 2 to 19, which in turn decreased the Al_2O_3 amount from 24.8 to 4.6 mol.%. The influence of cycle ratio on the phase composition and the mechanical properties throughout the thickness of the films were investigated. Since ZrO_2 thin films could be applicable in capacitor nanodevices, a common electrode material TiN was used as the substrate which also can affect the phase composition of the film.

Islands of metal oxide were fabricated on polycrystalline graphene (see Figure 4). Graphene was fabricated by CVD method and 5 ALD cycles of Al_2O_3 were done at room temperature to reduce damages to the graphene layer. Implementing only 5 cycles produces islands of Al_2O_3 on top of the graphene rather than a uniform layer. The islands of Al_2O_3 could potentially reinforce the defective grain boundaries of polycrystalline graphene. SiO_2 covered silicon substrate was used for graphene samples.

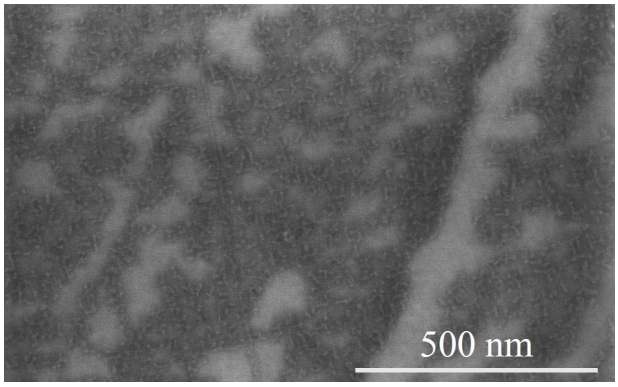

Figure 4. SEM image of 5 cycles of TMA + H_2O on graphene [**V**].

6. EXPERIMENTAL DETAILS

6.1 Atomic layer deposition

All the thin films analysed in this work were deposited at the Laboratory of Thin Film Technology at the University of Tartu by atomic layer deposition. Table 2 summarizes the used chemistry and deposition parameters.

Table 2. Atomic layer deposition process parameters.

Target material	Precursors	Reactor	Pulse times (s)	Deposition temperature	Growth rate (nm/cycle)	Engineer
Al_2O_3	$Al(CH_3)_3$ + H_2O	In-house built flow-type [65]	2-2-2-5	300 ºC	0.1	Taivo Jõgiaas Helle-Mai Piirsoo
		Picosun R200	0.3-4-0.3-6	22 ºC	–	Aivar Tarre
Ta_2O_5	$Ta(OC_2H_5)_5$ + H_2O	In-house built flow-type	2-2-2-5	300 ºC	0.07	Helle-Mai Piirsoo
ZrO_2	$ZrCl_4$ + H_2O	In-house built flow-type	4-3-2-5	300 ºC	0.07	Taivo Jõgiaas Aivar Tarre
SnO_2	SnI_4 + O_3	In-house built flow-type	5-2-5-5	300 ºC	0.21	Aivar Tarre

Table 3 depicts the deposition cycles of different samples discussed in this work. Sample designation used later in the work is established in Table 3. In addition, Table 3 holds the initial structural characterization parameters measured with X-ray reflectivity (XRR). Graphene was fabricated by CVD method on Cu foil in an in-house built reactor and transferred onto a SiO_2/Si substrate by Tauno Kahro (MSc). The thickness of SiO_2 was 300 nm.

6.2 X-ray diffraction and reflection

Crystal structures of the thin films were studied with grazing incidence XRD on Rigaku diffractometer. Table 4 depicts the critical angles for the studied materials and the used incidence angles. For some of the thin films depth-profiling was performed with GIXRD and, therefore, a range of angles was used. The periodic layered structure of laminates was determined with XRR with the same diffractometer combined with AXES modelling software [45]. The thicknesses of layers in nanolaminates are given in Table 3.

Table 3. Sample designations, their ALD cycles sequences and resulting layer thicknesses determined by XRR (error ± 1 nm).

Sample	Cycle sequences	Layered structure
$Si/Al_2O_3/Ta_2O_5$	$340\times(Al_2O_3) + 470\times(Ta_2O_5)$	Si/38/35 nm
$Si/Ta_2O_5/Al_2O_3$	$470\times(Ta_2O_5) + 340\times(Al_2O_3)$	Si/34/40 nm
$Si/Ta_2O_5/Al_2O_3/Ta_2O_5$	$313\times(Ta_2O_5)+227\times(Al_2O_3)+313\times(Ta_2O_5)$	Si/23/24/24 nm
$Si/Al_2O_3/Ta_2O_5/Al_2O_3$	$227\times(Al_2O_3)+313\times(Ta_2O_5)+227\times(Al_2O_3)$	Si/29/23/27 nm
$Si/(Al_2O_3/Ta_2O_5)\times2$	$2\times[170\times(Al_2O_3)+268\times(Ta_2O_5)]$	Si/19/19/19/20
$Si/SnO_2/ZrO_2$	$60\times(SnO_2) + 150\times(ZrO_2)$	Si/10/11 nm
$Si/ZrO_2/SnO_2$	$150\times(ZrO_2) + 60\times(SnO_2)$	Si/10/15 nm
Al_2O_3:ZrO_2 1:2	$400\times[1\times(Al_2O_3) + 2\times(ZrO_2)]$	Si/149 nm
1:4	$240\times[1\times(Al_2O_3) + 4\times(ZrO_2)]$	Si/114 nm
1:9	$120\times[1\times(Al_2O_3) + 9\times(ZrO_2)]$	Si/80 nm
1:14	$80\times[1\times(Al_2O_3) + 14\times(ZrO_2)]$	Si/83 nm
1:19	$60\times[1\times(Al_2O_3) + 19\times(ZrO_2)]$	Si/98 nm
Graphene/Al_2O_3	$5\times(Al_2O_3)$	–

Table 4. Critical angles of total external X-ray reflection of metal oxides (calculated and correlated to XRR results) and used incidence angles for GIXRD measurements on the studied samples. Signal depth is estimated using Equation 17. Errors due to X-ray beam scattering of 0.04°.

Sample	Critical angle α_c		Incidence angle α_i	Signal depth (nm)
Al_2O_3/Ta_2O_5 layers	Al_2O_3	0.28	0.50	850 ± 100
	Ta_2O_5	0.25	0.50	77 ± 9
Al_2O_3 doped ZrO_2	ZrO_2	0.30	0.28	5 ± 2
			0.30	13 ± 8
			0.32	25 ± 20
			0.34	40 ± 20
			0.45	110 ± 20
ZrO_2/SnO_2 layers	SnO_2	0.36	0.42	30 ± 5

6.3 Nanoindentation

Most of the nanoindentation measurements were done in CSM mode with Bruker Hysitron TriboIndeter TI980. Quasistatic nanoindentation was performed to correlate the results with CSM mode at very low loads and displacements. The maximum load applied by the probe was 10 mN, however, for the thin film characterization most measurements were carried out with 2 and 0.5 mN and for the thinnest films loads as low as 0.10 mN were implemented. On each sample about 30 separate indents were performed (see Figure 5), with outliers removed, often the geometric mean and standard deviation for hardness and Young's modulus were found with OriginLab software. The Young's modulus determined is the complex contact modulus. For at least 10 measurements of each patch unloading curve fitting according to Eq. 2 was performed with Hysitron TriboScan software to determine the h_f/h_{max} ratio of indents.

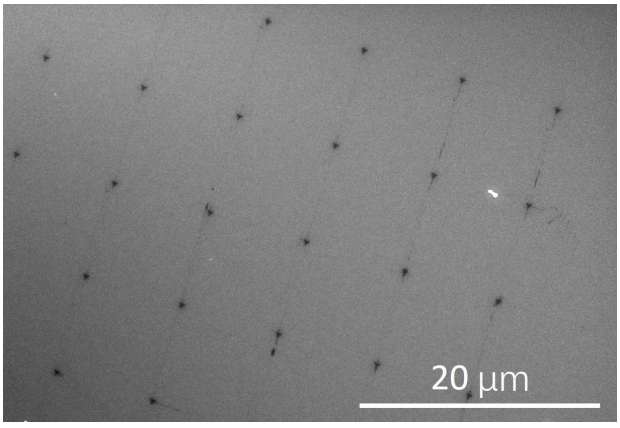

Figure 5. SEM image of a matrix of nanoindents on a thin film.

TriboIndenter implemented the Berkovich tip which was calibrated prior to the measurements (see section 2.2). The calibration entails the testing or renewing of the probe area function. For the fitting of the function ten or more CSM measurements with the load decreasing from 2 mN to 0.2 mN were done on fused quartz. To confirm the fit of the probe area function only a few CSM tests on fused quartz were necessary. The displacement range where proper values for the hardness and modulus of quartz were obtained were deemed reliable for measurements. Figure 6 depicts an example of such a calibration graph. The thin films measured had thickness around 20 nm, so the calibrated displacement range was as close to the surface as possible. From Figure 6 it can be seen that the modulus and hardness vary more at smaller displacements compared to at 40 nm. The irregularity and relatively high roundedness of the Berkovich tip, the surface roughness of samples and possibly the absence of plastic flow, decreased the accuracy of implementing the probe area function at displacements below 10 nm [66].

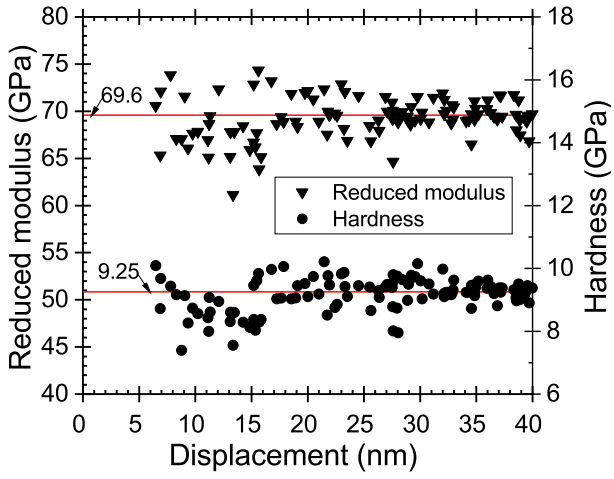

Figure 6. Results of nanoindentations on fused quartz sample with hardness 9.25 GPa and reduced (contact) modulus of 69.9 GPa to test the reliability of the probe area function in the displacement range below 40 nm [**IV**].

7. RESULTS

7.1 Al_2O_3 and Ta_2O_5 nanolaminates

7.1.1 As-deposited amorphous films

The hardness of 69 nm thick as-deposited amorphous Al_2O_3 reference film at a displacement of 10 nm reached 11.2 ± 1.0 GPa, whereas for 61 nm thick as-deposited amorphous Ta_2O_5 reference film it remained 8.2 ± 0.6 GPa. The difference of 3 GPa in the hardness of these two materials remains constant to the depth of 40 nm as shown in the hardness – displacement dependence in Figure 7. The Young's modulus of the Al_2O_3 and Ta_2O_5 were 154 ± 9 and 139 ± 5 GPa, respectively, at 10 nm and remained similar throughout the probed depth. The hardness and modulus of the Si substrate were 13.5 ± 0.4 and 147 ± 3 GPa, respectively [**I**].

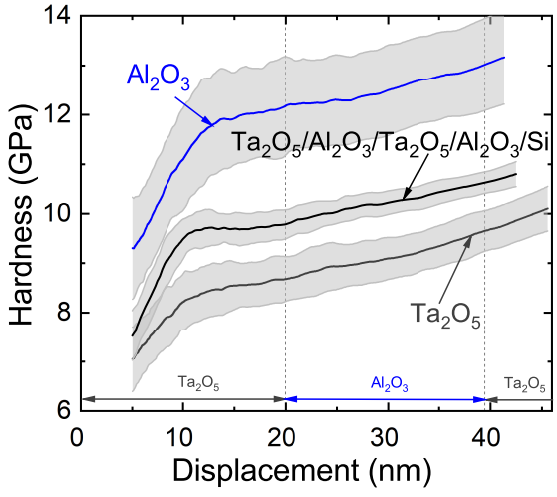

Figure 7. The hardness – displacement relationship of Al_2O_3 and Ta_2O_5 reference thin films and their laminate with four layers [**I**]. The thickness of single layers of the laminate in unstressed condition is indicated by the grey and blue horizontal arrows.

In Figure 8 the hardness – displacement relationship of as-deposited amorphous Al_2O_3 and Ta_2O_5 bilayers is shown. The thickness of the layers is depicted on the graph with gray and blue horizontal arrows. At the displacement of 10 nm the hardness (8.2 ± 0.6 GPa) of the bilayer with softer Ta_2O_5 on top resembles the hardness of the reference Ta_2O_5 film. At the displacement of 10 nm the hardness (10.4 ± 0.8 GPa) of the bilayer with the harder Al_2O_3 on top is, on average, lower compared to that of the reference Al_2O_3.

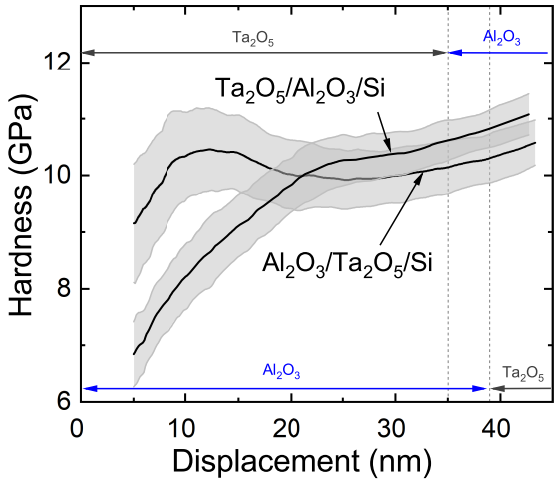

Figure 8. The hardness – displacement dependences of amorphous Al_2O_3–Ta_2O_5 bilayers [**I**]. The thickness of single layers in unstressed condition is indicated by the grey and blue horizontal arrows.

The hardness – depth dependence of $Al_2O_3/Ta_2O_5/Si$ bilayer possessed a wavy shape, with the maximum hardness of 10.5 GPa at 11 nm and the minimum hardness of 9.9 GPa at 25 nm. The hardness of the silicon substrate was 13.5 GPa and seemingly started to influence the measurements when the displacement into the film reached 25 nm, as counted from the surface, while the remaining distance to the film-substrate interface was still about 40 nm. The exact thickness of the layers under compression during the nanoindentation measurements remained unknown.

For the other bilayer, $Ta_2O_5/Al_2O_3/Si$, the hardness increased with depth. However, the slope of the curve fractions with almost linear rise of hardness against depth changed twice, creating three different regions. The intercepts and slopes of the linear regions at the highest displacements, at around 40 nm, coincided for both bilayers.

The hardness of as-deposited amorphous $Al_2O_3/Ta_2O_5/Al_2O_3$ and $Ta_2O_5/Al_2O_3/Ta_2O_5$ trilayers is shown in Figure 9, where it can be seen that the hardness – depth relationship of the nanolaminate containing two Ta_2O_5 layers possessed a wavelike shape similar to one in the case of bilayers. The hardness reached its maximum of 9.6 GPa at 15 nm and the minimum, 9.3 GPa, was reached at 25 nm. The maximum and minimum hardness values decreased with the layer thickness but were still reached at the same displacements. The hardness at the displacement of 10 nm was 8.7 ± 0.9 GPa which was slightly higher compared to that of the Al_2O_3/Ta_2O_5 bilayer with Ta_2O_5 layer on top.

For the $Al_2O_3/Ta_2O_5/Al_2O_3$ trilayer, the hardness was 9.9 ± 0.4 GPa at 10 nm, that is lower compared to the Al_2O_3/Ta_2O_5 bilayer with the top Al_2O_3 layer. However, at deeper displacements the hardness of the trilayer exceeded that of the $Al_2O_3/Ta_2O_5/Si$ stack. The hardness of the quad layer (four layers) in Figure 7

remained just slightly (~0.5 GPa) below that of the $Al_2O_3/Ta_2O_5/Al_2O_3$ trilayer throughout thickness.

At the same time, the elastic moduli of Al_2O_3 and Ta_2O_5 bilayers, trilayers, and the quad layer remained in a rather narrow range of 145 – 156 GPa throughout the probed thickness.

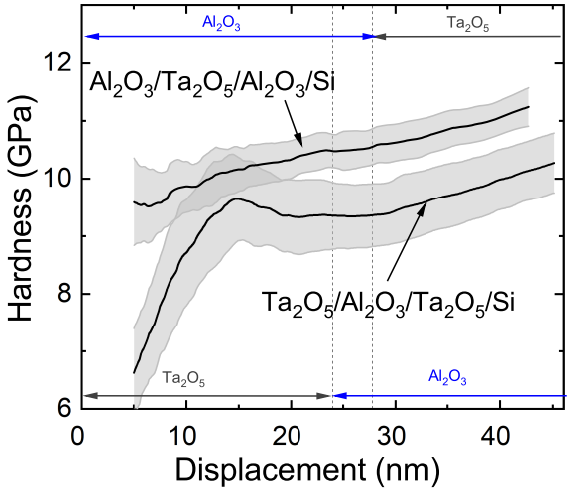

Figure 9. Hardness – displacement dependences of amorphous Al_2O_3–Ta_2O_5 trilayers [**I**]. The thickness of single layers in unstressed conditions is indicated by the grey and blue horizontal arrows.

7.1.2 Annealing induced changes to the structure

Annealing at 700 ºC caused changes in the microstructure of Al_2O_3/Ta_2O_5 bi- and trilayers, which became, besides XRD results, apparent from SEM images of the surfaces in Figure 10. Irregular grain-like features were observed on the surfaces of reference Ta_2O_5 film as well as $Ta_2O_5/Al_2O_3/Ta_2O_5$ trilayer. Relatively dark oblong surface features were also observed on the surface of the trilayer. Since the EDX analysis revealed a uniform distribution of elements, the image contrast between surface features was probably caused by different structural phases and the visible features are most likely crystallites of Ta_2O_5. On the surface of Al_2O_3/Ta_2O_5 bilayers, rare rectangular features with the size dependent on the sequence of the layers were observed, while the surface of the $Al_2O_3/Ta_2O_5/Al_2O_3$ trilayer remained unaffected by the treatment [**III**].

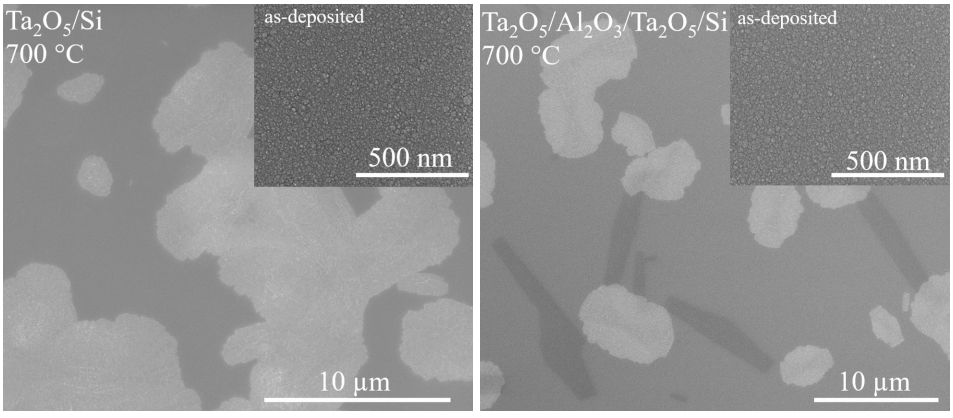

Figure 10. SEM images of as-deposited and annealed Ta_2O_5/Al_2O_3 thin films [**III**].

Annealing at 700 ºC resulted in orthorhombic Ta_2O_5 (PDF 00-025-0922) in the reference film and in the $Ta_2O_5/Al_2O_3/Ta_2O_5$ trilayer (Figure 11). The relative intensities of reflections of Si/Ta_2O_5 and $Si/Ta_2O_5/Al_2O_3/Ta_2O_5$ samples differed, indicating different preferential orientations for crystallites. Nanocrystals were detected in the $Al_2O_3/Ta_2O_5/Al_2O_3$ trilayer while bilayers remained X-ray amorphous with the treatment.

Annealing at higher temperature, i.e. 800 ºC, produced uniform surfaces for all the films with Ta_2O_5 on top (see Figure 12). The surface of reference Al_2O_3 and $Al_2O_3/Ta_2O_5/Si$ stack remained characteristic to the as-deposited materials, while the surface of the $Al_2O_3/Ta_2O_5/Al_2O_3$ trilayer exhibited some unique changes to the morphology (not shown) [**III**].

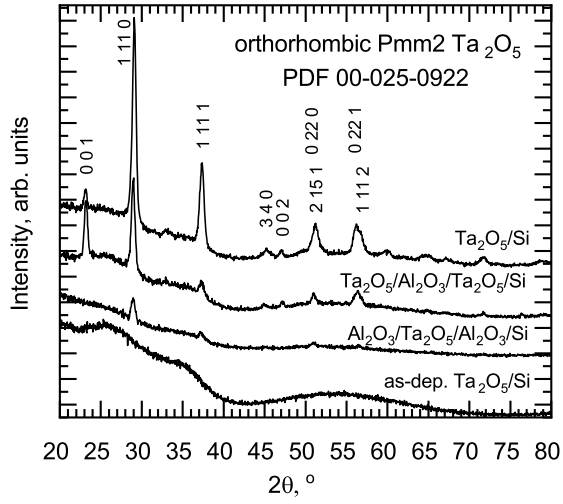

Figure 11. Diffractograms of as-deposited and annealed Ta_2O_5 reference film and annealed Al_2O_3 and Ta_2O_5 trilayers [**III**]. Annealing was carried out at 700 ºC for 10 min in air. GIXRD incidence angle α_i was equal to 0.50 degrees.

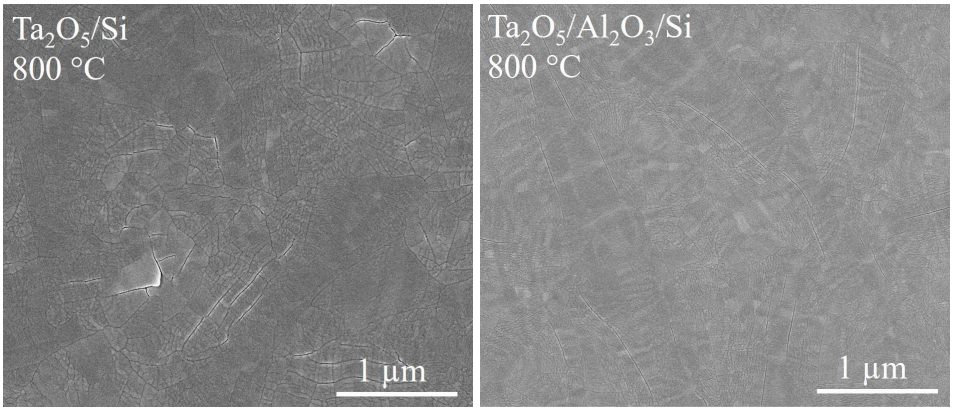

Figure 12. SEM images of annealed Ta_2O_5/Al_2O_3 thin films [**III**].

The uniform surfaces of crystallized Ta_2O_5 in Figure 12 exhibit cracks and more so in the reference Ta_2O_5 film. The surface of the samples was investigated with SPM (see Figure 13), where also the nanoindents are visible. The surface roughness was higher for the reference Ta_2O_5 compared to the bilayer.

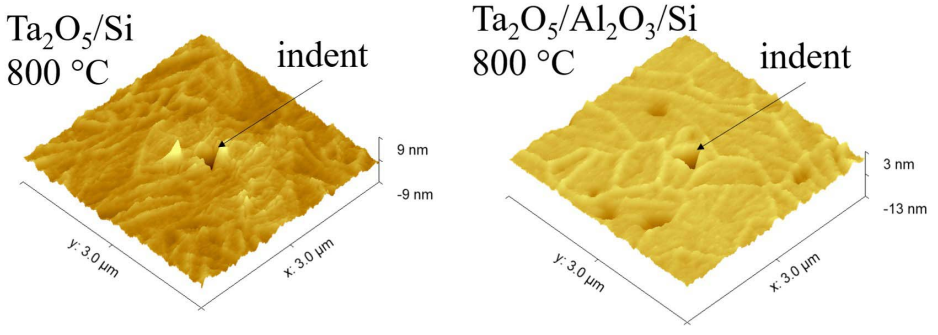

Figure 13. SPM images of the surface and nanoindents of annealed Ta_2O_5/Al_2O_3 thin films [**III**].

Figure 14a depicts the diffractograms for Ta_2O_5/Si, Ta_2O_5/Al_2O_3/Si and $Ta_2O_5/Al_2O_3/Ta_2O_5$/Si samples after 800 ºC. The latter, i.e. $Ta_2O_5/Al_2O_3/Ta_2O_5$ trilayer, possessed slightly lower relative intensities for 001 and 1 11 1 reflections compared to reference Ta_2O_5 and the bilayer. Figure 14b depicts the diffractograms for Al_2O_3/Si, Al_2O_3/Ta_2O_5/Si and $Al_2O_3/Ta_2O_5/Al_2O_3$/Si samples after 800 ºC. The relative intensity of the 001 reflection for the Al_2O_3/Ta_2O_5/Si stack was slightly lower compared to reference Ta_2O_5 and Ta_2O_5/Al_2O_3/Si stack. The diffractogram of the $Al_2O_3/Ta_2O_5/Al_2O_3$/Si nanolaminate differed significantly from that of the previously mentioned samples as its 001 reflection was nearly non-existent. Single reflection characteristic to γ-Al_2O_3 was measured for the reference Al_2O_3 film.

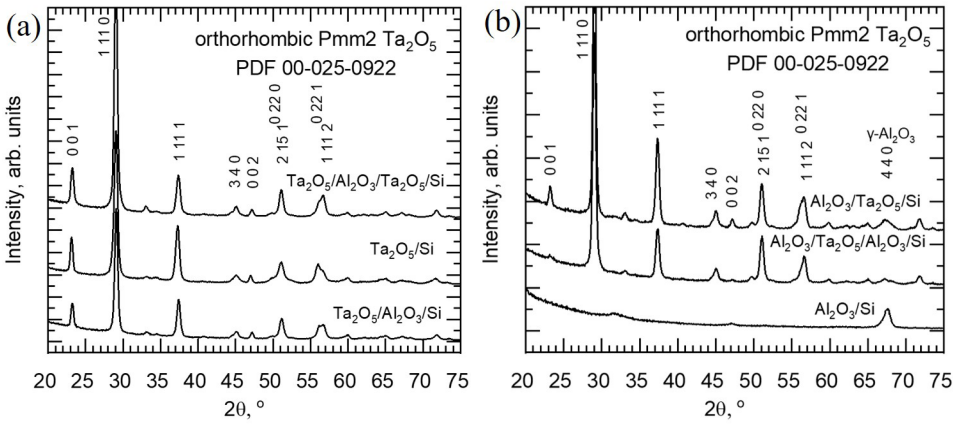

Figure 14. Diffractograms of annealed Ta_2O_5 reference film, Ta_2O_5/Al_2O_3 bilayer, and $Ta_2O_5/Al_2O_3/Ta_2O_5$ trilayer (a); Al_2O_3 reference film, Al_2O_3/Ta_2O_5 bilayer, and $Al_2O_3/Ta_2O_5/Al_2O_3$ trilayer (b) [**III**]. Annealing was carried out at 800 ºC for 10 min in air. GIXRD incidence angle α_i was equal to 0.50 degrees.

7.1.3 Mechanical properties of annealed films

The hardness of reference Ta_2O_5 increased to around 11.9 ± 2.8 GPa with crystallization and the individual nanoindentation measurements carried out on partially crystalline material annealed at 700 ºC gave divergent results (see Figure 15).

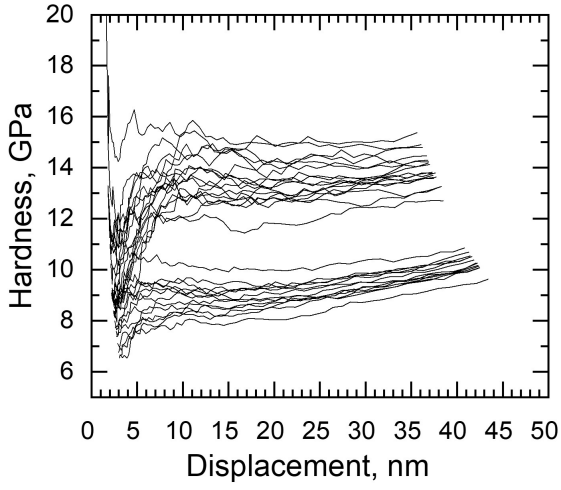

Figure 15. Hardness – displacement relationship of amorphous Ta_2O_5 thin film after annealing at 700 ºC. 30 nanoindentation measurements were carried out in sequence and are depicted in the present graph.

Additionally, to compare the influence of layer thickness on the structure and mechanical properties, the Ta_2O_5 reference film with smaller thickness, 43 nm, was characterized with nanoindentation after annealing at 800 ºC. At the displacement of 10 nm the hardness reached 13.5 ± 1.5 GPa. The SEM surfaces and diffractograms resembled that of the 69 nm thick Ta_2O_5 annealed film. The comparable hardness at the displacement of 36 nm for the thicker Ta_2O_5 film was 13.1 ± 2.5 GPa [**III**]. Annealing increased the hardness of reference Al_2O_3 from 11 to 18 GPa, even as no crystallization occurred. Moduli of the references increased to about 155 and 170 GPa for Ta_2O_5 and Al_2O_3, respectively, after annealing at 800 ºC [**III**].

Figure 16 depicts the hardness – depth dependencies of the annealed bi- and trilayers. The figure differs from the conventional nanoindentation graph configuration as the axes are switched to better visualize the artificial periodic structure of the nanolaminates along the depth of the measurement. Annealing at 700 ºC had little influence on the hardness of the laminates. The hardness just seemed to slightly increase in the vicinity of the very surface, most apparently for the Al_2O_3/Ta_2O_5/Si stack. The graph retained its wavy shape, as did the graph of the Ta_2O_5/Al_2O_3/Ta_2O_5 trilayer. The annealing created a wave shape for the Al_2O_3/Ta_2O_5/Al_2O_3 trilayer as well.

After annealing at 800 ºC the hardness reached the highest value, 16 GPa, for the bilayer with top Ta_2O_5 layer and did not vary throughout the probed depth (Figure 16). The hardness of the Al_2O_3/Ta_2O_5/Si stack remained around 14 GPa throughout the thickness of the film. The hardness of both annealed trilayers remained around 13 GPa even as they consisted of different fractions of Al_2O_3 and Ta_2O_5. Overall, the hardness – displacement dependence seemed to flatten with annealing (Figure 16). The Young's moduli of the laminates increased by ~5 GPa after 700 ºC and only up to 170 GPa after 800 ºC [**III**].

The scanning probe microscopy of nanoindents on the as-deposited and annealed Al_2O_3/Ta_2O_5 samples did not detect pile-up (Figure 13). Figure 17 shows the h_f/h_{max} ratios of single indents made on all the aforementioned samples. All the values remained below 0.7 indicating no pile-up and, therefore, the correctness of the area function implemented. The h_f/h_{max} ratios coincided for Ta_2O_5 and Al_2O_3 before and after annealing, even as annealing uniformly decreased the ratio for all samples.

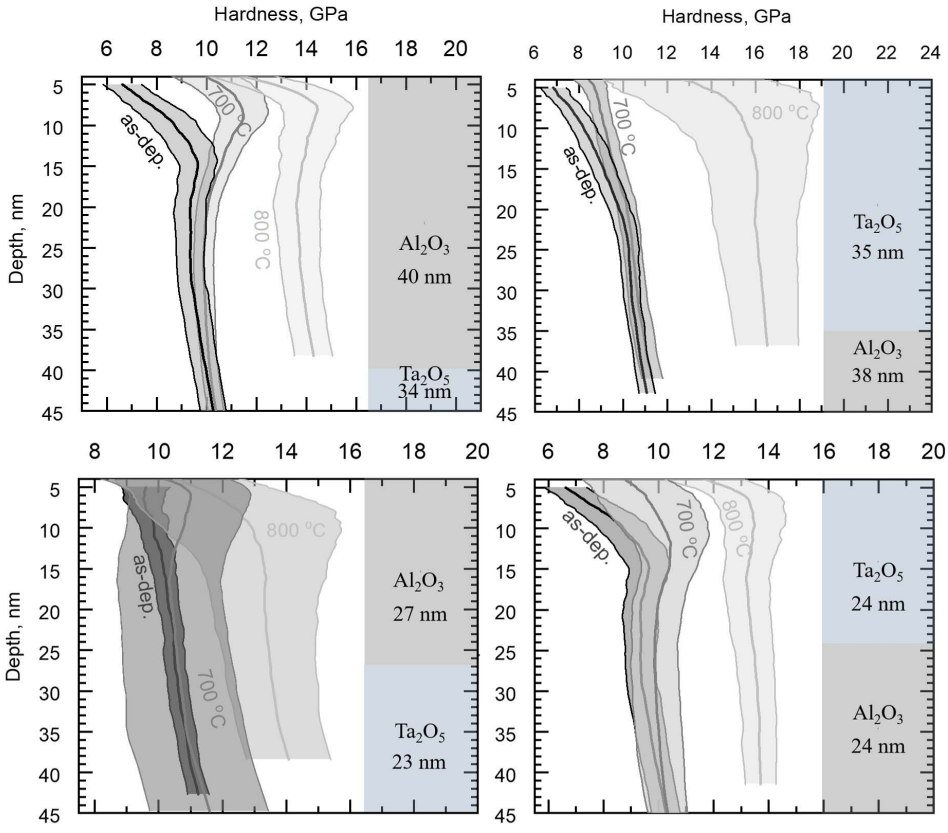

Figure 16. The hardness – depth dependence of as-deposited and annealed Al_2O_3/Ta_2O_5 nanolaminates. The periodic layer structure is shown on the right.

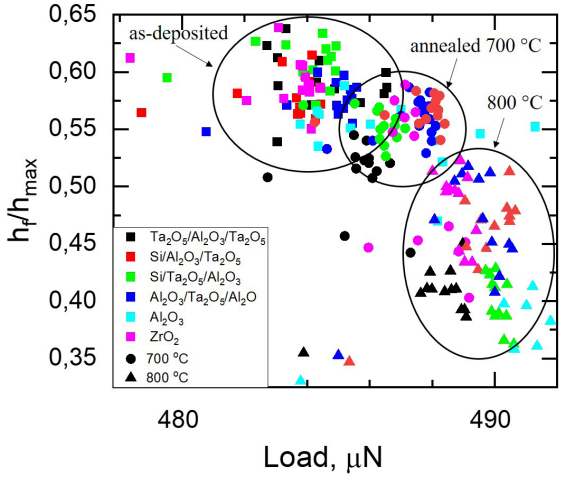

Figure 17. Unloading curve analysis results for as-deposited and annealed Al_2O_3/Ta_2O_5 thin films. Nanoindentation was performed in CSM mode with maximum load set to 0.5 mN.

7.2 Alumina doped zirconia thin films

The addition of Al_2O_3 in ZrO_2 films promoted the formation of tetragonal and cubic phases (Figure 18), instead of the monoclinic and tetragonal phase mixture determined in the reference ZrO_2. The cycle ratio of 19:1, when applied for the growth of ZrO_2:Al_2O_3 mixture films (see Table 3), produced a film crystallized in tetragonal and, possibly, complementary cubic phase of ZrO_2, which contained 2.8 at.% of Al. GIXRD depth profiling revealed consistent phase composition throughout the thickness of the film [**II**]. Application of cycle ratios 14:1 (3.5 at.% of Al) and 9:1 (4.8 at.% of Al) produced cubic ZrO_2 and further increase of Al_2O_3 content (≥6.5 at.% of Al) resulted in completely X-ray amorphous materials. Depth-profiling of the cubic films revealed the formation of preferential orientation of crystallites constituting the solid film, that, however, varied with depth. In Figure 18 the change of relative intensity of 111_C and 200_C reflections with depth is apparent for the sample grown using the cycle ratio of 14:1. Less distinct, yet similar change of I_{111}/I_{200} with depth was present for samples grown using cycle ratios of 19:1 and 9:1 [**II**].

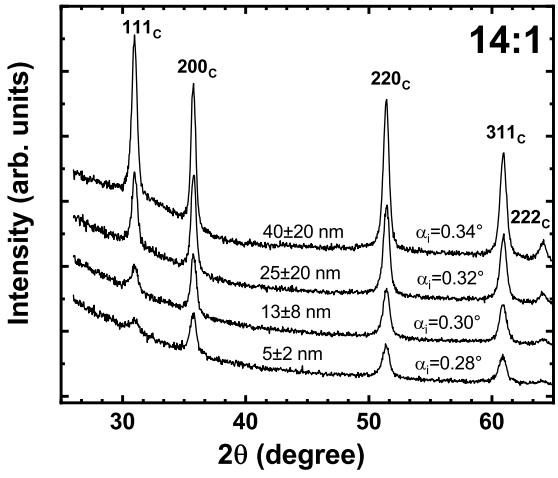

Figure 18. Grazing incidence XRD in profiling mode for thin film deposited with ZrO_2:Al_2O_3 cycle ratio of 14:1. Reflections of cubic ZrO_2 are denoted. Incidence angles and corresponding X-ray penetration depths in nanometers are indicated at each diffractogram [**II**].

The hardness of the reference 100 nm thick ZrO_2 film grown and formed as a solid layer in monoclinic/tetragonal mixed phase was 12.2 ± 1.4 GPa at the indentation depth of 30 nm and increased to 13.3 ± 1.1 GPa at the depth of 70 nm. The hardness of the TiN/Si substrate was 12.6 GPa. The amorphous doped ZrO_2 films were softer compared to the reference and substrate. The highest hardness, 15.1 ± 0.5 GPa, was determined in the films grown using the cycle ratio of 14:1 at 70 nm. The thickness of the film was 83 nm and the hardness value, as measured, remained stable throughout the thickness of the film even as the hardness

of the substrate was 2.5 GPa lower (Figure 19). The 98 nm thick sample grown using cycle ratio of 19:1 possessed on average 1 GPa lower hardness compared to the sample grown using cycle ratio of 14:1. The depth dependence of the hardness was, however, analogous in both cases (Figure 19). The most significant change in hardness along the indentation depth was measured for 83 nm thick sample grown using the cycle ratio of 9:1, where the hardness value of 13.1 ± 1.7 GPa at 30 nm rose to 14.7 ± 1.0 GPa at 70 nm. Doping increased the elastic modulus to 162–171 GPa at 30 nm, compared to that of 127 GPa that was measured for reference ZrO_2. The modulus decreased with the increase in depth in the crystalline doped films, as expected, as the modulus of the substrate was 148 GPa. The modulus of the amorphous Al_2O_3:ZrO_2 films, however, retained values near 160 GPa even at 70 nm [**II**].

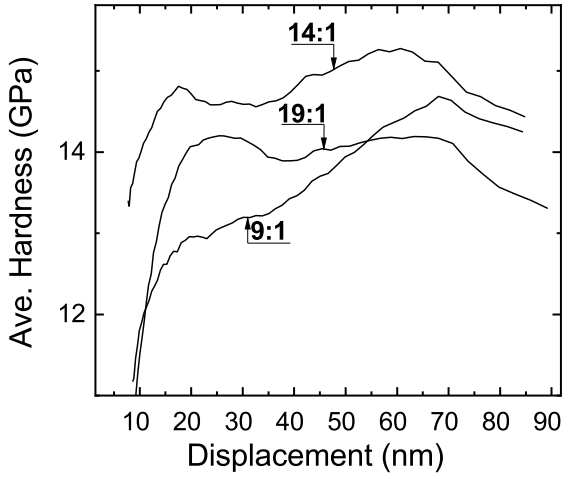

Figure 19. Hardness – displacement dependence of three Al_2O_3 doped ZrO_2 films consisting of tetragonal/cubic phases of ZrO_2 [**II**].

The unusual behaviour of the hardness – displacement relationship of the sample grown with cycle ratio 14:1 was investigated further with the Puchi-Cabrera model for coating hardness (see section 2.3). The 10 nm thick TiN layer did not fit into the model, so the hardness of the substrate was set to 12.6 GPa which was measured at 30 nm into the TiN/Si substrate. The averaged hardness values in the range from 30 to 80 nm was used for fitting as tests on fused quartz showed correct values in the displacement range (see Figure 20).

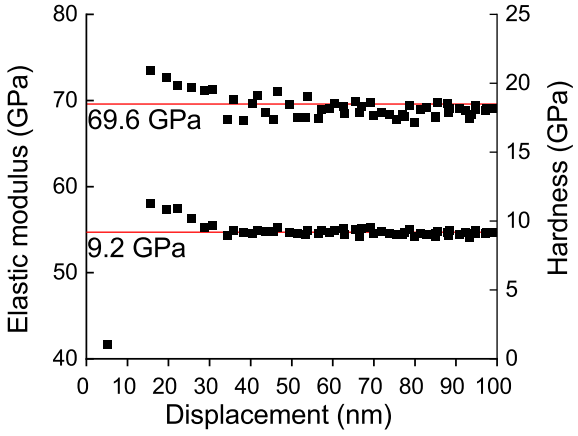

Figure 20. Nanoindentation measurements on fused quarts [**II**].

Figure 21 shows the fitting results for four different layer architectures that are described in detail in Table 5. Fitting A describes the hardness – displacement relationships of a single layer film – substrate system and its poor fit confirmed that the hardness of the film changes with depth. The other three models resulted in similar curves even as the layer architectures differed. Fitting B describes the hardness of two distinct layers of equal thickness (H_1=14.8 and H_2=16.4 GPa), while fitting C describes the hardness of two distinct layers with fitted varying thicknesses (H_1=14.8 and H_2=15.5 GPa) (see Table 5). The three-layered architecture with fixed equal thicknesses (H_1=15.0, H_2=14.0 and H_3=16.8 GPa) resulted in a similar curve and goodness of fit. All models showed an average hardness around 16 GPa near the substrate and about 14 GPa near surface.

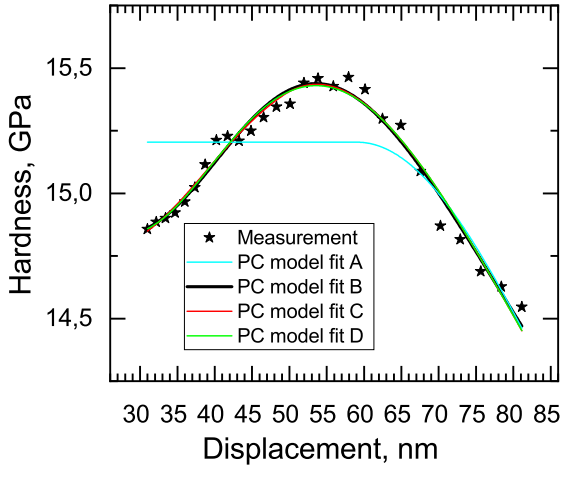

Figure 21. Puchi-Cabrera multilayer model fittings for the hardness of 83 nm thick textured ZrO_2:Al_2O_3 thin film grown with 14:1 cycle ratio. Fitting parameters are brought in Table 5.

Table 5. Fitting parameters of Puchi-Cabrera multilayer hardness model for ZrO_2:Al_2O_3 thin film grown with 14:1 cycle ratio.

Parameter	A	B	C	D
Number of layers with distinct hardness in the film	1	2	2	3
1st layer thickness (from surface)	83 nm (fixed)	41.5 (fixed)	28 nm	27 nm (fixed)
2nd layer thickness	–	41.5 (fixed)	55 nm	27 nm (fixed)
3rd layer thickness (near substrate)	–	–	–	29 nm (fixed)
1st layer hardness (GPa)	15.2	14.8	14.8	15.0
2nd layer hardness (GPa)	–	16.4	15.5	14.0
3rd layer hardness (GPa)	–	–	–	16.8
1st layer constant K	0.71	0.67	0.93	0.57
2nd layer constant K	–	0	0.42	0.005
3rd layer constant K	–	–	–	0.49
1st layer constant β	0.45	0.51	0.65	0.50
2nd layer constant β	–	0.77	0.57	0.59
3rd layer constant β	–	–	–	0.69
Coefficient of determination (R^2)	0.50	0.97	0.96	0.97

The constants K for the second layer converged to zero for B fitting and close to it for D fitting (see Table 5). Puchi-Cabrera *et al.* analysis for diamond-like-carbon, CrC and CNiPCr multilayer coating resulted in values varying from 0.01 to 0.41 for K and 0.313 to 0.428 for β for single layers [30]. That analysis implemented a Vickers tip, wider displacement range and the layer thicknesses were 900 nm or several magnitudes thicker. Goodness of fit indicates that the model might be applicable also in conditions used in this study. Constant K, that describes the influence from underlaying material (see section 2.3), might behave differently in the case of very thin layers where substrate influence is more prevalent.

In the case of very thin film, smaller measurement range is used as the tip is more accurately calibrated in smaller sections. However, as shown in Figure 22 the Puchi-Cabrera model could potentially predict hardness closer to the surface even from the given data. The model gave varying results for surface hardness depending on the periodic layered structure. From the additional measurement points it would seem as the curve D is more accurate as it shows the increase in hardness. However, it cannot be said for certain that the measurement is true as the calibration graph in Figure 20 shows that the used tip area function over-estimated the hardness of the fused quartz at displacements shallower than 30 nm.

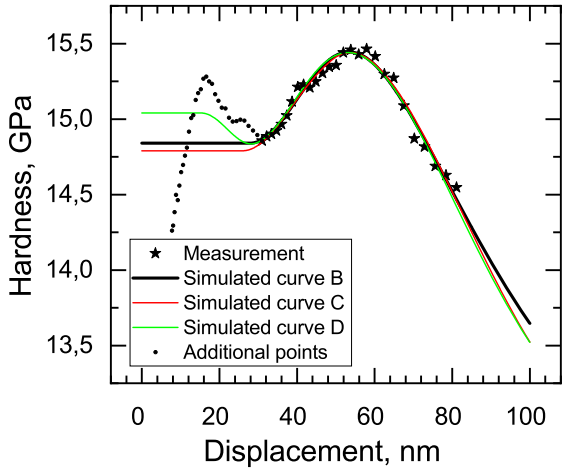

Figure 22. Predictions for possible surface hardness for the ZrO_2:Al_2O_3 thin film grown with 14:1 cycle ratio based on Puchi-Cabrera two (B,C) and three (D) layer models. Measurement points used for fitting are designated with star signs, while additional non-calibrated measurements are shown with dots.

Figure 23 depict the h_f/h_{max} ratios for ZrO_2:Al_2O_3 thin films. On average, all the films possess slightly different ratios, unlike in the case of Al_2O_3 and Ta_2O_5 nano-laminates. The h_f/h_{max} remained below 0.7 for all.

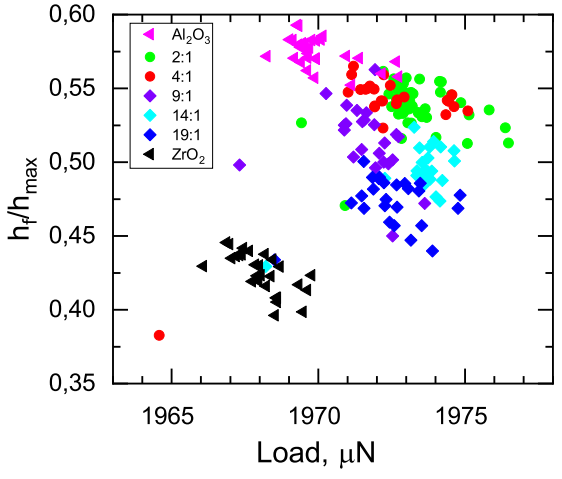

Figure 23. Unloading curve analysis results for Al_2O_3 doped ZrO_2 thin films. Nano-indentation was performed in CSM mode with maximum load set to 2 mN.

7.3 Very thin SnO_2 and ZrO_2 bilayers

The hardness of 21 nm thick tetragonal ZrO_2 film was 11.5 ± 1.1 GPa, as measured into the depth ranging from 10 to 30 nm. For the 25 nm thick SnO_2 film consisting of a mixture of orthorhombic and tetragonal phases (Figure 24), the hardness reached 14.8 ± 1.1 GPa in the same displacement range (not shown) [**IV**]. The difference in the hardness values was, thus, about 3 GPa for these two materials.

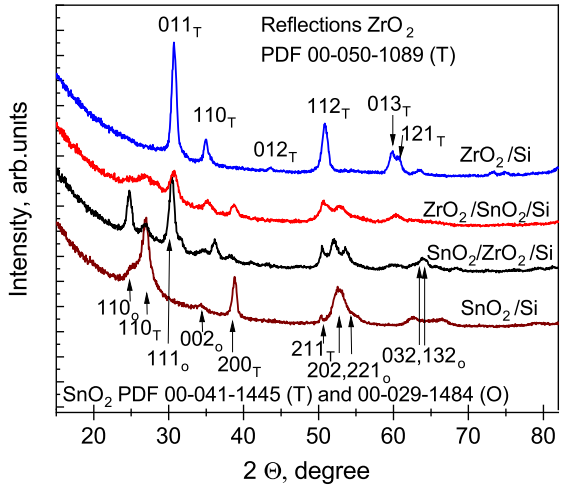

Figure 24. Diffractograms of atomic layer deposited ZrO_2 and SnO_2 thin films and bilayers **[IV]**.

The bilayers of ZrO_2 and SnO_2 exhibited reflections characteristic to tetragonal ZrO_2, orthorhombic SnO_2, and tetragonal SnO_2 (Figure 24). The hardness – displacement relationship of the bilayers is shown in Figure 25, and on average, the hardness of the SnO_2/ZrO_2 bilayer with the interfacial ZrO_2 and top SnO_2 layer grown on Si was higher than that of the $ZrO_2/SnO_2/Si$ stack. The hardness value, as measured, was 15.1 ± 1.1 GPa, with the minimum and maximum of 11.6 and 20.0 GPa, respectively. The hardness value stayed stable, apparently, throughout the thickness of the films.

The elastic modulus of 21 nm thick tetragonal ZrO_2 film was determined to be 96 ± 1 GPa in the same depth range. Modulus reached 175 ± 1 GPa for the 25 nm thick SnO_2 film (not shown) [**IV**]. The difference of modulus was about 80 GPa for these two materials.

The modulus – displacement relationship of the bilayers is also shown in Figure 25, where the elastic modulus of the $SnO_2/ZrO_2/Si$ stack is significantly higher compared to the alternative configuration of layers. The modulus was 171 ± 1 GPa, with the minimum and maximum of 143 and 205 GPa, respectively. The $ZrO_2/SnO_2/Si$ stack, however, exhibited more uniform values, with the minimum and maximum of 62 and 89 GPa, respectively. The modulus stayed stable throughout the thickness of the films similarly to hardness.

As expected, the ratio h_f/h_{max} was < 0.7 as the substrate was softer and did not promote pile-up. The ratio varied similarly for all samples and loads (Figure 26).

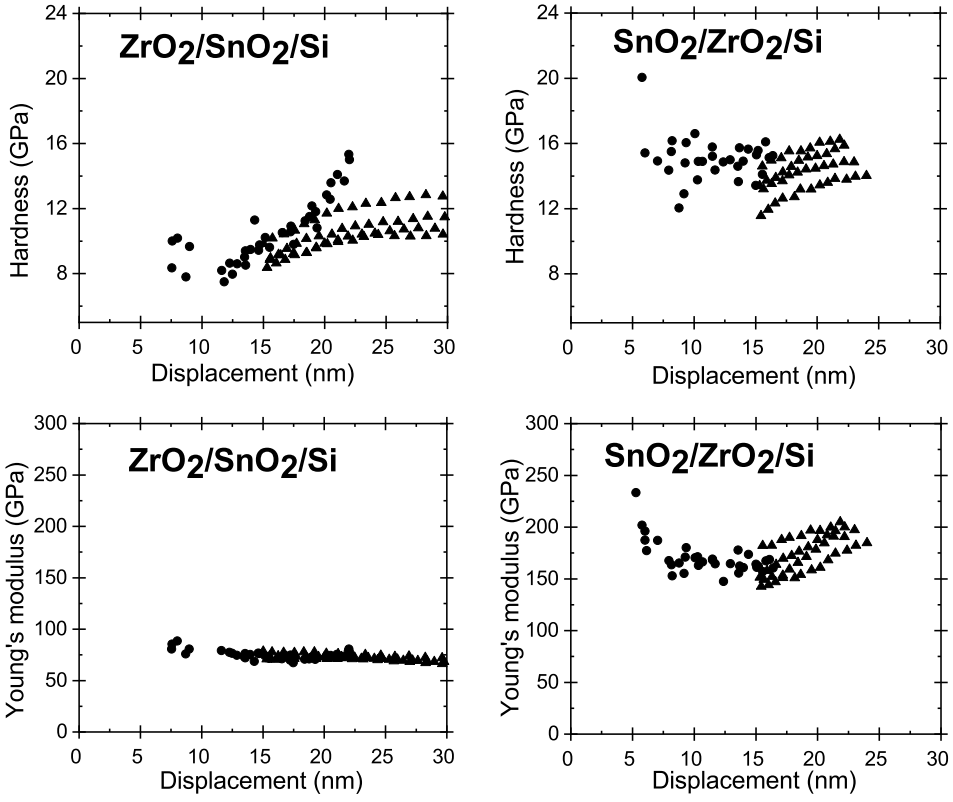

Figure 25. The hardness – displacement and elastic modulus – displacement relationships of ZrO_2 and SnO_2 bilayers [**IV**]. Nanoindentation were done in quasistatic (●) and CSM (▲) modes.

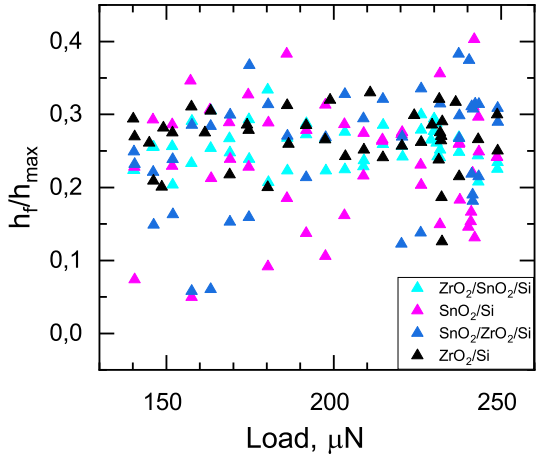

Figure 26. Unloading curve analysis results for ZrO_2 and SnO_2 thin films. Nanoindentation was performed in CSM and quasistatic mode with varying loads above 140 μN.

7.4 Reinforcement of graphene with ALD

The addition of five ALD cycles of Al_2O_3 on graphene on SiO_2/Si substrate increased the materials Young's modulus from 96 to 125 GPa at maximum indentation depth. The hardness and elastic modulus of samples containing graphene increased with indentation load [**V**]. The Al_2O_3/graphene composite possessed an improved elastic recovery capability compared to the references. Nanoindents were made with loads up to 10 mN and characterized with SPM afterwards. The Berkovich tip applied only 0.5 µN during the SPM scans, so the final depths of indents could be estimated (see Figure 27). The final depth of an indent is shallower than the contact depth used for calculations because elastic recovery occurs after load withdrawal. The recovery seemed to be significant, almost 50% higher, for the reinforced graphene at 5 mN compared to the Si/SiO_2/graphene stack.

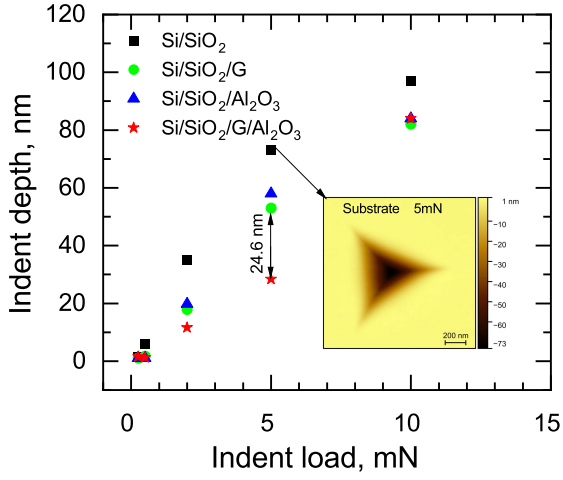

Figure 27. SPM measured final depth of indents for substrate, graphene, 5 cycles of Al_2O_3, and Al_2O_3 reinforced graphene [**V**]. The maximum depths reached during loading were comparable for these samples.

Figure 28 depicts the h_f/h_{max} ratios for all the samples at all loads. It was observed that the ratio varied a lot between individual indents at low loads, yet did not differ between the samples. The h_f/h_{max} ratio increased with load as the contact of the indent became more plastic, especially for graphene containing samples. The elasticity and plasticity of graphene seems dependent on the applied load and ALD.

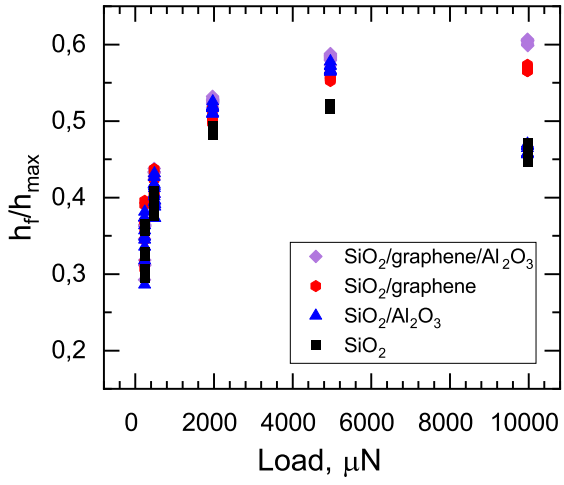

Figure 28. Unloading curve analysis results for graphene and Al_2O_3 composites. Nano-indentation was performed in CSM mode with varying loads.

8. DISCUSSION

8.1 Reinforcement of the softer functional material by restricting its deformation

As-deposited Al_2O_3 and Ta_2O_5 thin films possessed a difference in hardness of about 3 GPa and in Young's modulus of about 15 GPa. The elastic modulus of their nanolaminates did not vary with depth, sequence of constituent layers or volume fraction. The elastic modulus of a coating is more sensitive to the influences from a substrate during nanoindentation, compared to the hardness [22]. It would seem that the difference in moduli was too small to strengthen the material in any capacity and an elastically homogenous coating was produced. In comparison, nanoindentation done by Coy *et al.* [15] on TiO_2/Al_2O_3 nanolaminates on Si substrates showed that the elastic modulus depended on the laminate architecture and indenter displacement into the 100 nm thick film, while the difference in moduli between the constituents was only 7 GPa . In those TiO_2/Al_2O_3 thin films one of the components, TiO_2, was in crystalline form. However, the TiO_2/Al_2O_3 nanolaminates deposited by Ylivaara *et al*. [14] were mostly amorphous, and the constituents possessed an even lower difference in elastic modulus – 4 GPa, while the nanolaminate architecture did not influence the elastic modulus significantly. The elastic modulus was dependent on the volume fractions of TiO_2 and Al_2O_3, though. Most significant influence on the elastic modulus from the artificial periodic structure was achieved by Homola *et al*. [20] with 200 nm thick ZnO/Al_2O_3 thin films, where the constituents possessed no difference in their Young's moduli, while the elastic moduli of the nanolaminate with 2 nm thick single layer period exceeded that of the constituents by more than 10 GPa at the displacement of 20 nm. The structure of ZnO was determined crystalline in that nanolaminate. Thus, based on the previous reports as well as on the findings in the present study, the elastic modulus of ALD-grown metal oxides can be increased in multilayers with artificial architecture, provided that one of the component oxides is crystalline. Combining amorphous materials retains more homogeneous elasticity through composite films.

The hardness of the completely amorphous Al_2O_3 and Ta_2O_5 nanolaminates deposited in this study did vary slightly with volume fraction, depth and architecture. As expected, the hardness depended on the volume fractions of constituents. At displacements of 20 nm or deeper the bilayers of equal volume fractions possessed quite similar hardness (Figure 8). The trilayer, consisting of multiple Al_2O_3 layers, hardened at deeper displacements. The trilayer, consisting of multiple Ta_2O_5 layers, was the softest (Figure 9), compared to other multilayers. The quadlayer, consisting of equal amounts of Ta_2O_5 and Al_2O_3, demonstrated monotonous increase in hardness, very similarly to the $Al_2O_3/Ta_2O_5/Al_2O_3/Si$ stack (Figure 7). The hardness of the quadlayer at the entire displacement range fell between the values characterizing of the two bilayers. This is indicative of the possibility to

modify the hardness of such thin films with the layer architecture of multilayers consisting of stacked component films with distinct composition.

Earlier, the hardness of amorphous TiO_2/Al_2O_3 thin films, where the constituents possessed the hardness difference of 2 GPa, have not varied significantly with the artificial architecture, but varied with volume fraction [14]. The hardness of crystalline TiO_2 and amorphous Al_2O_3 nanolaminates has varied slightly with architecture even as the constituents separately possessed the difference as small as 1.2 GPa [15]. Crystalline ZnO and amorphous Al_2O_3 nanolaminates with a specific artificial periodicity hardened by several GPa compared to either of the reference films [20].

Similarly to elastic modulus, the hardness of ALD metal oxide composite thin film could be modified more easily with the presence of a crystalline constituent. The plastic flow in an ordered lattice occurs via dislocation glide which can be hindered at interfaces between constituent layers in a composite. When combining amorphous materials, higher difference in the plasticity of constituents could provide better control over the composite hardness with nanolaminate architecture. Since the plastic flow in amorphous materials occurs by random shear atomic rearrangements, it is more difficult to hinder it by interfaces.

Next to dense crystalline oxide layers with tunable thickness, performance of two-dimensional crystals, typically represented by graphene, in stacks with amorphous components appeared as phenomenon worth investigations and reporting. The elastic modulus of graphene/SiO_2/Si system was slightly increased with ALD at higher loads. The elastic recovery of graphene on SiO_2 was shown to improve with Al_2O_3 at higher loads (Figure 27). Load dependency of the mechanical properties could be related to graphene wrinkling during transfer to the SiO_2 substrate. At higher loads the graphene is stretched out under the indenter and its effects on the measurement could become more prominent.

A possible mechanism that increases the elasticity of graphene by ALD could be the reinforcement of the defective grain boundaries of the CVD produced polycrystalline graphene. Numerical and experimental studies have shown that graphene grain boundaries can be defective and weaken the material's strength and elasticity compared to pristine graphene [61–62]. The Al_2O_3 islands on top of the graphene "stitch" grains together. It has been shown that polycrystalline CVD graphene with well-stitched grains can achieve the strength of a pristine graphene [61]. Possibly, ALD can be used to enhance the mechanical properties of CVD graphene.

8.2 Doping induced phase transformation and preferred orientation

The investigations considering the Puchi-Cabrera composite hardness model (Figure 21, Table 5) showed that the ZrO_2:Al_2O_3 thin film deposited with 14:1 cycle ratio did not possess a steady hardness throughout the thickness, but rather a gradual increase of hardness with the depth. There are several possible causes

for that kind of behaviour, such as Al_2O_3 content, phase composition or texture variations throughout the thickness.

The dopant incorporation distribution with atomic layer deposition possesses periodicity, depending on the cycle sequences as determined earlier with STEM-EDX for TiO_x:Nb [43] and atom probe tomography for ZnO:Al [67]. It is reasonable to assume that in the present study, for the given sample referred to above, the used cycle sequence of $80\times[1\times(Al_2O_3) + 14\times(ZrO_2)]$ would create quite homogeneous Al_2O_3 distribution of 3.5 at.% throughout the thickness and would not cause such hardness.

Moderate, rather small, Al_2O_3 content in the film can promote the stabilization of relatively hard cubic ZrO_2 phase. It has been shown that the dopant type and amount can significantly affect the strength, and therefore the hardness, of cubic ZrO_2 [68]. This is probably why the hardness as low as 15.1 GPa was achieved for cubic thin films, which is below that of the previously reported 20 GPa [56].

Amorphous, monoclinic, tetragonal and cubic phases of ZrO_2 exhibit rise in their hardness, in the same order, from 5 to 20 GPa [57, 69–70]. The phase composition of ALD ZrO_2 films depends on the thickness. At the beginning of the deposition, the surface energy of the amorphous phase is the lowest until the thickness exceeds 10 nm, after which the cubic/tetragonal growth starts to prevail. Eventually, with thickness over 50 nm, dominantly monoclinic ZrO_2 will be deposited [40, 70–71]. GIXRD depth profiling performed on all the crystalline films did show the same phases throughout the depth (Figure 18). However, XRD cannot account for the amorphous phase. Even extensive transmission electron microscopy studies would not confidently determine the volume fraction of the amorphous phase. Passing the solubility limit of Al_2O_3 in ZrO_2 could increase the amorphous phase fraction in the film as the incorporation of 6.5 at.% of Al resulted in completely X-ray amorphous films, while the next lower tested amount of 4.8 at.% of Al resulted in cubic ZrO_2 thin film that possessed the highest rise in hardness with displacement (sample 9:1 in Figure 19). However, since Al_2O_3 concentration should be uniform in the film, the amount of amorphous phase due to the doping should be distributed evenly along the depth as well. The amorphicity induced during the initial stages of deposition would mean that the hardness would decrease near the substrate, but the opposite was actually the case (Figure 19).

The most likely cause for the hardness – displacement behaviour is the preferential orientation of crystallites, i.e. texture. Preferential orientation has been prevalent in atomic layer deposited ZrO_2 thin films, as reported in several studies earlier [19, 40, 72–74]. Deposition parameters such as temperature, precursors chemistry, substrate and number of cycles have affected the texture of un-doped ZrO_2. Formation of preferential orientation during ALD could be related to the differences of surface energies of different crystallographic planes of a lattice, cubic or monoclinic. This could affect the precursor adsorption and diffusion rates and ultimately different growth rates for planes could develop. The plane with the highest growth rate will cause the texture by creating the biggest grains with the plane parallel to the surface [71, 75]. In the current study, it was shown that Al_2O_3 doping can influence, in addition to the phase composition, the texture

as well. It has been shown numerically that the dopant type and amount in cubic ZrO_2 can affect the structure (bond strength, length, angle) of the crystallographic planes [68]. This could possibly influence the texture development process as, in the present study, the texture changed with film thickness (Figure 18), probably because the surface energies and growth rates change with thickness similarly as the phase composition of ZrO_2 thin films change with thickness. A numerical study has shown that, e.g., the ideal strength of yttria doped cubic ZrO_2 differed along different crystallographic directions, i.e. the material is anisotropic [68]. It could be concluded that the gradual change of texture throughout the thickness of the film causes the gradual increase of hardness.

Previously, the possibilities to modify the texture of ALD-grown metal oxide thin film in order to engineer their mechanical properties, have been studied. Graphene and Al_2O_3 interlayers have been implemented to induce suitable texture in ZnO thin films for better tribological properties [12, 18]. Texture modification could be implemented to create even harder metal oxide thin films for MEMS applications.

For SnO_2/ZrO_2 bilayers, the difference in their diffractograms is apparent (Figure 24), indicating that the deposition order of oxide layers has significantly influenced the structure of constituents during ALD. This might be the main cause of the significant dependence of hardness on the layer sequence. The softer ZrO_2 on top of SnO_2 might be more amorphous compared to the reference film as the layer thickness is low, only 11 nm (see Table 3) and very thin ZrO_2 ALD films are mostly amorphous as mentioned above [40]. Softer film on top can flow freely during nanoindentation and lower the hardness compared to the ZrO_2 reference, causing the reinforcement of the underlaying SnO_2 not to be as significant (Figure 25). Softer film – harder substrate system can be prone to pile-up (see section 2.2). However, for the $ZrO_2/SnO_2/Si$ stack, both SPM and h_f/h_{max} (Figure 26) exhibited no pile-up. It could be that in the case of that small material volumes the pile-up processes might not be significant.

In the case of the double layer consisting of metal oxide layers deposited in the opposite order, the hardness of the bilayer resembled that of the reference SnO_2, possibly because the material was more crystalline as the XRD reflections were more intense compared to the other bilayer (Figure 24). The slightly harder SnO_2 layer on top of the softer ZrO_2 can restrict the plastic flow in the underlayer and cause the higher hardness of the double-layered film through the depth (Figure 25).

Even when the hardness difference of constituents was the same, 3 GPa, for both SnO_2/ZrO_2 and Ta_2O_5/Al_2O_3 bilayers, the hardness – displacement relationships were more stable throughout the thickness for the SnO_2/ZrO_2 bilayers (Figure 25, Figure 8). The uniform hardness of SnO_2/ZrO_2, as measured, could appear due to the shorter layer period compared to Ta_2O_5/Al_2O_3 nanolaminate periods (10 vs 34 nm, see Table 3) or changes in the phase composition compared to the reference films.

The amorphous structure of Al_2O_3 and Ta_2O_5 was not interrupted with different substrates when layering on top of each other, whereas the crystal structure

of SnO_2 and ZrO_2 was affected by the substrate and/or layer thickness. This would mean that the indentation results obtained from the reference SnO_2 and ZrO_2 films did not represent the actual mechanical properties of the constituents in their bilayers as the degree of crystallization and phase composition of both oxides influenced their properties. The hardness difference between the SnO_2/ZrO_2 bilayer constituents could be lower than 3 GPa, in reality.

The hardness of SnO_2/ZrO_2/Si stack was comparable to that of the reference SnO_2 film, unlike the Ta_2O_5/Al_2O_3 amorphous bilayers that were softer compared to the reference Al_2O_3. It has been shown that the layer period, interface sharpness and difference of constituent's elastic moduli, affect the strengthening effects in heterostructures [32]. Young's moduli differed about 80 and 15 GPa, respectively, for SnO_2/ZrO_2 and Ta_2O_5/Al_2O_3. The overall hardening effect of SnO_2 on ZrO_2 compared to Al_2O_3 on Ta_2O_5 could have been the results arising from the differences in moduli.

However, the properties measured from the thin reference SnO_2 and ZrO_2 films might not represent the actual values of the moduli of the constituents in bilayers. The bilayers consisting of SnO_2 and ZrO_2 possessed architecture dependent Young's moduli, unlike the Ta_2O_5/Al_2O_3 nanolaminates (Figure 25). Very little variance and steady value along displacement was measured for the ZrO_2/SnO_2/Si stack, indicating certain possibility for the growth of mechanically isotropic material. The modulus of the thicker reference ZrO_2 thin film in previous ZrO_2:Al_2O_3 study was 30 GPa higher compared to the thinner reference ZrO_2 film. The Young's modulus of ZrO_2 was significantly affected by the phase composition of the film, which, in turn, can be dependent on the thickness.

In addition, the strengthening effect can be more significant on crystalline materials like SnO_2/ZrO_2 bilayers than completely amorphous Al_2O_3/Ta_2O_5 ones as discussed in section 8.1.

8.3 Annealing induced crystallization

SEM and GIXRD studies (Figure 10, and Figure 11, respectively) allowed one to describe Ta_2O_5 surface, partially crystallized after annealing at 700 ºC. Nanoindentation measurements confirmed the formation and presence of morphologically non-homogenous surface as two separate hardness values were registered (Figure 15). It appears likely, that the nanoindentations on the amorphous areas of Ta_2O_5 give the lower hardness values around 8 GPa, whereby the measurements on crystallized areas give higher values around 13 GPa. Crystallization at 800 ºC produced uniform surface and its average hardness coincided with the upper section hardness of the partially crystallized Ta_2O_5. Figure 15 also illustrates the trend that the hardness varies more in the polycrystalline materials (ΔH= ~3 GPa) compared to amorphous ones (ΔH= ~1 GPa).

Annealing at 700 ºC caused crystallization of Ta_2O_5 in Al_2O_3/Ta_2O_5 trilayers, yet not in bilayers (Figure 11). This was supported by SEM studies as grain-like surface features appeared more prominent in trilayers. Another indication of

crystallization, apparent only in trilayers, can be seen in Figure 16, where the hardness after annealing at 700 ºC varied more for the trilayers than bilayers. Contradictorily, crystallization temperature has been shown to increase as film thickness or layer period decreases. For instance, thin Al_2O_3 films start crystallizing at 800 ºC when their thickness exceeds 10 nm [49], while in a ZnO/Al_2O_3 laminate the 20 nm thick Al_2O_3 layers have remained amorphous after annealing at 800 ºC for 10 min [76]. Extensive study on the post-deposition annealing of amorphous SiO_2/ZrO_2 nanolaminates was conducted by Larsen *et al*. [63]. The layer period of SiO_2 was kept constant at 2 nm, while ZrO_2 period decreased from 27 to 1 nm. The nanolaminates were annealed at temperatures in the range of 300–900 ºC with a 50 ºC ascending step. Crystallization temperature of ZrO_2 increased with decreasing ZrO_2 period. The amount of ZrO_2 crystallization per annealing temperature and layer period was determined and it was deduced that higher number of layers leads to more intense crystallization while the overall content of ZrO_2 remains same in the films. It was proposed that higher ZrO_2 crystallization in the laminates with higher number of layers, and therefore interfaces, could mean there are more crystallization seeds present [63]. This appears to be the case also in the present study as the layer period of tri- and bilayers differs about 33% (Table 3), while the trilayers contain Ta_2O_5 – Al_2O_3 interfaces with area twice as large as that in the double layers, which could provide markedly more nuclei for the Ta_2O_5 crystallization. The architecture of nanolaminates could, thus, be modified in order to usefully influence the crystallization temperature of the constituent metal oxides.

Annealing induced formation of differently shaped grains (Figure 10) and caused variations in relative intensities of reflections in diffractograms (Figure 11, Figure 14), influenced by Ta_2O_5/Al_2O_3 laminate artificial periodic structure. The grain shape and relative intensities of reflections can be indicative of the occurrence of texture in the thin films. For a parallel from the literature, a preferential orientation was determined in ZnO layers in ZnO/Al_2O_3 laminates after post-deposition annealing at 800 ºC for 10 min [76].

Texture could be the reason why the bilayers have possessed different hardness (Figure 16). Similarly, trilayers with different constituent volume fractions possess hardness below that of the bilayers after annealing at 800 ºC. The standard deviation of hardness of $Ta_2O_5/Al_2O_3/Si$ and $Al_2O_3/Ta_2O_5/Al_2O_3/Si$ stacks was higher compared to the other two nanolaminates after annealing at 800 ºC (Figure 16). Nanoindentation of a polycrystalline material yields high variance in measurements as the measurements are highly localized and the orientation of a single grain right under the tip could influence the mechanical property [77]. If the material was textured, the orientation of grains would not vary as much and so the variance between single nanoindentation measurements could be supressed. The lower hardness and its variance in the $Al_2O_3/Ta_2O_5/Si$ and $Ta_2O_5/Al_2O_3/Ta_2O_5/Si$ stacks could be the result of a preferred orientation with lower strength.

To conclude, the artificial periodic structure of metal oxide nanolaminates can be engineered to modify the physical, particularly mechanical, properties of thin films by inducing crystallization with preferred orientation of grains.

8.4 Influence of residual stresses in the film

The hardness of annealed Ta_2O_5/Al_2O_3 bilayers depended on the deposition order of the constituents (Figure 16). The difference in hardness could be caused by the presence of internal stresses. Tensile residual stresses in thin films have been shown to significantly depend upon the layer architecture in TiO_2/Al_2O_3 nanolaminates [13–14]. Compressive stresses could potentially increase the hardness of a material as there has been correlation between compressive stresses and hardness in magnetron sputtered coatings [33]. Tensile stress in a material could cause cracking. In the present study, SEM and SPM studies revealed cracks in Ta_2O_5 surfaces, emerged after annealing at 800 ºC (Figure 12, Figure 13). These cracks probably weakened the material and lowered the hardness. The hardness of crystalline Ta_2O_5 films has previously been reported to be higher, around 14 GPa, compared to the 12 GPa measured in the present study. Referring to the literature, magnetron sputtered 15 µm thick textured orthorhombic Ta_2O_5 coating was measured to be as hard as 14.3 ± 0.4 GPa, while in the same study the hardness of an amorphous 500 nm thick Ta_2O_5 film was 8.2 ± 0.4 GPa [55], which is a value very similar to that determined in the present study for amorphous Ta_2O_5 (Figure 7). The 15 µm thick coating was annealed at 1000 ºC for an hour and the hardness, consequently, decreased to 9.3 ± 0.5 GPa. The change in hardness was attributed to recrystallization and reduction in stresses [55]. The Young's modulus of the magnetron sputtered Ta_2O_5 in the latter study varied between 139 and 188 GPa [55], which is quite similar to the values measured for ALD Ta_2O_5 films in the present study (see section 7.1.1). The hardness of 14.6 ± 1.3 GPa was measured for nanocrystalline Ta_2O_5 in another study as well [78]. The lower hardness of 11.9 GPa measured in the present work could be the result of stress-induced cracks. Both SEM and SPM surface scans revealed that the crack development could be not as prominent in bi- and trilayers with Ta_2O_5 on top, compared to the reference Ta_2O_5 film. Underlaying Al_2O_3 could help to reduce stress in Ta_2O_5 and, therefore, lower amounts of structural defects in the material would develop. That would increase the hardness of the $Ta_2O_5/Al_2O_3/Si$ stack (Figure 16). Simply reducing the reference Ta_2O_5 thin film thickness did not influence hardness, which means that the layer thickness alone does not significantly affect the mechanical properties. However, the artificial periodic structure of a nanolaminate allows one to modify the hardness.

9. CONCLUSIONS

In this study, the structure and mechanical behaviour of atomic layer deposited amorphous and annealed crystalline Ta_2O_5/Al_2O_3 nanolaminates, as-deposited crystalline SnO_2/ZrO_2 bilayers, Al_2O_3-doped ZrO_2 thin films and an Al_2O_3/graphene composite layers were investigated. It was shown that the artificial periodic structure of nanocomposite thin films can affect their mechanical properties.

It was found that the artificial periodic architecture, in addition to the volume fraction of amorphous constituents in Al_2O_3/Ta_2O_5 nanolaminates affects the hardness of thin solid films. The reinforcement of an artificial periodic architecture can become more significant if one or both of the nanolaminate components were crystalline, most prominently demonstrated in the case of bilayers of SnO_2 and ZrO_2 bilayers. The interfaces between constituent oxides probably disrupt dislocation glide expected in nanocrystalline component layers rather than randomized amorphous flow only possible in structurally completely disordered constituents. The Young's modulus was also affected by the nanolaminate architecture when the constituents were crystalline SnO_2 and ZrO_2, but not in the completely amorphous Al_2O_3/Ta_2O_5 nanolaminates.

The elastic modulus, hardness and elastic recovery of graphene/SiO_2/Si stack was improved with five cycles of atomic layer deposited Al_2O_3 as, quite possibly, the ALD helped to reinforce the defective grain boundaries of CVD graphene.

Post-deposition annealing caused changes to the morphology and structure of Ta_2O_5/Al_2O_3 nanolaminates that depended on the periodic architecture. It was shown that the layer thickness, number of interfaces and the order of constituent layers can determine the crystallization temperature and the preferential orientation of Ta_2O_5 crystallites. In addition, tensile and compressive residual stresses probably generated during phase transformations in the thin films could affect their mechanical behaviour. Nanolaminate structure can be used to modify the crystal structure and possibly stress levels, consequently modifying the hardness of thin films.

Doping ZrO_2 with Al_2O_3 during the atomic layer deposition process allowed one to modify the phase composition and texture of the thin films. This was shown to affect the mechanical hardness of the material. The maximum hardness of 15.1 GPa was measured for the cubic ZrO_2 thin film containing 3.5 at.% of Al and the hardness changed throughout the thickness of the film together with the preferential orientation of grains.

The results show possible ways to modify the mechanical properties of ALD metal oxide thin films, in order to design nanocomposites suited, for instance, to MEMS technologies.

SUMMARY IN ESTONIAN

Kunstlikult valmistatud perioodilise struktuuriga nanokomposiitide mehhaanilised omadused

Mikroelektromehaaniliste süsteemide (MEMS) ja teiste nanoseadmete valmistamiseks on vajalikud mehaaniliselt vastupidavad kiled ja muud nanomaterjalid. Käesolevas töös uuriti võimalusi modifitseerida aatomkihtsadestatud metalloksiidkiledest nanokomposiitide mehaanilisi omadusi. Sadestamisel muudeti kunstlikku perioodilist laminaatarhitektuuri, varieerides komponentkihtide paksusi ja sadestamise järjekorda, et takistada pehmema komponendi deformatsiooni, mõjutada komponentide faasikoostist ja tekstuuri sadestamise järejekorraga, dopeerimisega või sadestuse järgsel lõõmutamisel või mõjutada kiledes esinevaid sisepinged.

Aatomkihtsadestatud amorfsete Al_2O_3/Ta_2O_5 kaksik- ja kolmikkihtidest koosnevate 70 nm kogupaksusega laminaatkilede kõvadus oli vähesel määral mõjutatud lamineeritud komponentkihtide perioodist, samas nende nanolaminaatide Young'i moodul ei varieerunud üldse. Perioodilise kunstliku kihilise struktuuri vähene mõju amorfsete Al_2O_3/Ta_2O_5 nanolaminaatide mehaaniliste omadustele võis olla tingitud piirpindade vähesest takistusest materjali plastsele voolamisele kile pinnatasandi sihis, mis muidu toimub korrapäratus segumaterjalis.

Nende Al_2O_3/Ta_2O_5 kilede lõõmutamisel toimusid muutused morfoloogias ja kristallstruktuuris, mille ulatus sõltus komponentkihtide järjekorrast. Nanolaminaadi arhitektuur mõjutas oluliselt Al_2O_3/Ta_2O_5 kilede kõvadust pärast lõõmutamist, sest ilmselt kihtide järjekord mõjutas kristalliitide kuju ja/või materjalikihis või kihtide piirpindadel tekkinud sisepingeid.

Polükristalse struktuuriga 20 nm paksuste SnO_2/ZrO_2 kaksikkihtide kõvadus ja elastsusmoodul sõltusid oluliselt komponentide järjekorrast. Sadestus järjekord mõjutas komponentide kristallstruktuuri, mis omakorda võis põhjustada mehaaniliste omaduste varieerumise. Mehaanilistele omadustele võis lisaks mõju avaldada piirpind kristallstruktuuriliselt osaliselt korrastatud komponentkihtide vahel, takistades dislokatsioonide libisemist nanokristallilistes materjalides.

Aatomkihtsadestamine võimaldas modifitseerida SiO_2 alusele sadestusjärgselt üle viidud, eelnevalt keemilise aurufaassadestus meetodil sünteesitud polükristalse grafeeni mehaanilisi omadusi. Grafeeni pinnale sadestatud Al_2O_3 saarekesed tõstsid materjali elastsusmoodulit ja parandasid elastsust peale nanotäkkimist. Sadestatud Al_2O_3 saarekesed võisid täita ja kompenseerida polükristallilisele grafeenile iseloomulike joondefekte ehk üksikute liblede vahelisi piirpindu, tugevdades struktuuri tervikuna.

Aatomkihtsadestusel dopeeriti ZrO_2 kilesid Al_2O_3-ga, et soodustada kuubilise meta-stabiilse ja monokliinse faasiga võrreldes mehaaniliselt kõvaema faasi teket. Maksimaalne kõvadus 15.1 GPa mõõdeti kuubilise ZrO_2 kile korral, kus alumiiniumi sisaldus ulatus väärtuseni 3.5 at.%. Kiles kasvu jooksul moodustunud kristalliitidel kujunes eelisorientatsioon, mis ilmselt mõjutas materjali kõvadust.

Uurimistöö tulemused näitasid, et metalloksiididest koosnevate õhukeste kilede faasikoostist ja tekstuuri on võimalik erinevate parameetritega (lisandelemendid, alus, paksus, kunstlik perioodiline arhitektuur, lõõmutmine) kontrollida ning seega kilede mehaanilisi omadusi modifitseerida, pidades silmas võimalikke tuleviku-rakendusi näiteks MEMS-struktuuridel.

ACKNOWLEDGEMENTS

I would like to thank my supervisors, dr. Taivo Jõgiaas, dr. Aile Tamm and prof. Kaupo Kukli, who made an excellent supervising team. We had educational and exciting discussions over the mechanical properties of thin films and how to manipulate them with Taivo almost daily since the beginning of my doctoral studies. It was one of my favourite parts of the studies and probably quite constructive to our research. Aile had a huge influence on my confidence as she explained the administrative parts of the job and how to properly present and promote my research. Taivo and Aile both taught me how to inspire and supervise younger students. Kaupo helped me develop my writing skills and was a hugh support as a deep well of knowledge and experience.

I am thankful to assoc. prof. Hugo Mändar, who helped carry out extensive X-ray diffraction measurements and analysis. I appreciate all the support and guidance I received from my other colleagues. I would like to thank Mrs. Alma-Asta Kiisler, Mr. Aivar Tarre, Mr. Peeter Ritslaid, Mr. Tauno Kahro, Dr. Aarne Kasikov and Dr. Jekaterina Kozlova. Acknowledgements to co-authors Mr. Joosep Link and Dr. Raivo Stern as well.

I would like to wish strength to my fellow PhD students, Markus, Mahtab, Joonas and Elyad, who shared and understood the struggle.

REFERENCES

[1] W. Song *et al.*, "Analog switching characteristics in TiW/Al_2O_3/Ta_2O_5/Ta RRAM devices," *Appl. Phys. Lett.*, vol. 115, no. 13, p. 133501, Sep. 2019, doi: 10.1063/1.5100075.

[2] M. A. Jenkins, D. Z. Austin, K. E. K. Holden, D. Allman, and J. F. Conley, "Laminate Al_2O_3/Ta_2O_5 Metal/Insulator/Insulator/Metal (MIIM) Devices for High-Voltage Applications," *IEEE Trans. Electron Devices*, vol. 66, no. 12, pp. 5260–5265, Dec. 2019, doi: 10.1109/TED.2019.2948140.

[3] B. V. T. Hanby, B. W. Stuart, M. Gimeno-Fabra, J. Moffat, C. Gerada, and D. M. Grant, "Layered Al_2O_3-SiO_2 and Al_2O_3-Ta_2O_5 thin-film composites for high dielectric strength, deposited by pulsed direct current and radio frequency magnetron sputtering," *Applied Surface Science*, vol. 492, pp. 328–336, Oct. 2019, doi: 10.1016/j.apsusc.2019.06.202.

[4] Y.-H. Wu, C.-K. Kao, B.-Y. Chen, Y.-S. Lin, M.-Y. Li, and H.-C. Wu, "High density metal-insulator-metal capacitor based on ZrO_2/Al_2O_3/ZrO_2 laminate dielectric," *Appl. Phys. Lett.*, vol. 93, no. 3, p. 033511, Jul. 2008, doi: 10.1063/1.2958238.

[5] H. Song, D. Kim, S. Kang, H. Jung, H. Lim, and K. Yong, "Al_2O_3 blocking layer inserted ZrO_2 Metal-Insulator-Metal capacitor for the improved electrical and interfacial properties," *Thin Solid Films*, vol. 713, p. 138368, Nov. 2020, doi: 10.1016/j.tsf.2020.138368.

[6] G. T. Dahl *et al.*, "Alumina-Doped Zirconia Submicro-Particles: Synthesis, Thermal Stability, and Microstructural Characterization," *Materials*, vol. 12, no. 18, Art. no. 18, Jan. 2019, doi: 10.3390/ma12182856.

[7] J. Merisalu *et al.*, "Structure and Electrical Properties of Zirconium-Aluminum-Oxide Films Engineered by Atomic Layer Deposition," *Coatings*, vol. 12, no. 4, Art. no. 4, Apr. 2022, doi: 10.3390/coatings12040431.

[8] Y. Huang, A. Sai Sarathi Vasan, R. Doraiswami, M. Osterman, and M. Pecht, "MEMS Reliability Review," *IEEE Transactions on Device and Materials Reliability*, vol. 12, no. 2, pp. 482–493, Jun. 2012, doi: 10.1109/TDMR.2012.2191291.

[9] B. Bhushan, "Nanotribology and nanomechanics of MEMS/NEMS and BioMEMS/BioNEMS materials and devices," *Microelectronic Engineering*, vol. 84, no. 3, pp. 387–412, Mar. 2007, doi: 10.1016/j.mee.2006.10.059.

[10] L. Kilpi *et al.*, "Tribological properties of thin films made by atomic layer deposition sliding against silicon," *Journal of Vacuum Science & Technology A: Vacuum, Surfaces, and Films*, vol. 36, no. 1, p. 01A122, Jan. 2018, doi: 10.1116/1.5003729.

[11] S. Shestaeva *et al.*, "Mechanical, structural, and optical properties of PEALD metallic oxides for optical applications," *Appl. Opt.*, vol. 56, no. 4, p. C47, Feb. 2017, doi: 10.1364/AO.56.000C47.

[12] I. Iatsunskyi *et al.*, "Influence of ZnO/graphene nanolaminate periodicity on their structural and mechanical properties," *Journal of Materials Science & Technology*, vol. 34, no. 9, pp. 1487–1493, Sep. 2018, doi: 10.1016/j.jmst.2018.03.022.

[13] L. Ghazaryan *et al.*, "Structural, optical, and mechanical properties of TiO_2 nanolaminates," *Nanotechnology*, vol. 32, no. 9, p. 095709, Feb. 2021, doi: 10.1088/1361-6528/abcbc1.

[14] O. M. E. Ylivaara *et al.*, "Aluminum oxide/titanium dioxide nanolaminates grown by atomic layer deposition: Growth and mechanical properties," *Journal of Vacuum Science & Technology A: Vacuum, Surfaces, and Films*, vol. 35, no. 1, p. 01B105, Jan. 2017, doi: 10.1116/1.4966198.

[15] E. Coy, L. Yate, Z. Kabacińska, M. Jancelewicz, S. Jurga, and I. Iatsunskyi, "Topographic reconstruction and mechanical analysis of atomic layer deposited Al_2O_3/TiO_2 nanolaminates by nanoindentation," *Materials & Design*, vol. 111, pp. 584–591, Dec. 2016, doi: 10.1016/j.matdes.2016.09.030.

[16] T. Jõgiaas *et al.*, "Mechanical properties of aluminum, zirconium, hafnium and tantalum oxides and their nanolaminates grown by atomic layer deposition," *Surface and Coatings Technology*, vol. 282, pp. 36–42, Nov. 2015, doi: 10.1016/j.surfcoat.2015.10.008.

[17] T. Jõgiaas, M. Kull, H. Seemen, P. Ritslaid, K. Kukli, and A. Tamm, "Optical and mechanical properties of nanolaminates of zirconium and hafnium oxides grown by atomic layer deposition," *Journal of Vacuum Science & Technology A: Vacuum, Surfaces, and Films*, vol. 38, no. 2, p. 022406, Mar. 2020, doi: 10.1116/1.5131563.

[18] S. A. Alvi, P. Ghamgosar, F. Rigoni, A. Vomiero, and F. Akhtar, "Adaptive nanolaminate coating by atomic layer deposition," *Thin Solid Films*, vol. 692, p. 137631, Dec. 2019, doi: 10.1016/j.tsf.2019.137631.

[19] T. Jõgiaas, R. Zabels, A. Tarre, and A. Tamm, "Hardness and modulus of elasticity of atomic layer deposited Al_2O_3-ZrO_2 nanolaminates and mixtures," *Materials Chemistry and Physics*, vol. 240, p. 122270, Jan. 2020, doi: 10.1016/j.matchemphys.2019.122270.

[20] T. Homola *et al.*, "Mechanical properties of atomic layer deposited Al_2O_3/ZnO nanolaminates," *Surface and Coatings Technology*, vol. 284, pp. 198–205, Dec. 2015, doi: 10.1016/j.surfcoat.2015.07.078.

[21] W. C. Oliver and G. M. Pharr, "Measurement of hardness and elastic modulus by instrumented indentation: Advances in understanding and refinements to methodology," *J. Mater. Res.*, vol. 19, no. 1, p. 18, 2004. https://doi.org/10.1557/jmr.2004.19.1.3

[22] A. C. Fischer-Cripps, "Critical review of analysis and interpretation of nanoindentation test data," *Surface and Coatings Technology*, vol. 200, no. 14, pp. 4153–4165, Apr. 2006, doi: 10.1016/j.surfcoat.2005.03.018.

[23] G. M. Pharr and A. Bolshakov, "Understanding nanoindentation unloading curves," *Journal of Materials Research*, vol. 17, no. 10, pp. 2660–2671, Oct. 2002, doi: 10.1557/JMR.2002.0386.

[24] W. J. Wright and W. D. Nix, "Storage and loss stiffnesses and moduli as determined by dynamic nanoindentation," *Journal of Materials Research*, vol. 24, no. 3, pp. 863–871, Mar. 2009, doi: 10.1557/jmr.2009.0112.

[25] E. G. Herbert, W. C. Oliver, and G. M. Pharr, "Nanoindentation and the dynamic characterization of viscoelastic solids," *J. Phys. D: Appl. Phys.*, vol. 41, no. 7, p. 074021, Mar. 2008, doi: 10.1088/0022-3727/41/7/074021.

[26] A. Bolshakov and G. M. Pharr, "Influences of pileup on the measurement of mechanical properties by load and depth sensing indentation techniques," *Journal of Materials Research*, vol. 13, no. 4, pp. 1049–1058, Apr. 1998, doi: 10.1557/JMR.1998.0146.

[27] A. A. Pelegri and X. Huang, “Nanoindentation on soft film/hard substrate and hard film/soft substrate material systems with finite element analysis,” *Composites Science and Technology*, vol. 68, no. 1, pp. 147–155, Jan. 2008, doi: 10.1016/j.compscitech.2007.05.033.

[28] X. Chen and J. J. Vlassak, “Numerical study on the measurement of thin film mechanical properties by means of nanoindentation,” *J. Mater. Res.*, vol. 16, no. 10, pp. 2974–2982, Oct. 2001, doi: 10.1557/JMR.2001.0408.

[29] S. Zhang, Ed., “Nanostructured Thin Films and Coatings: Mechanical Properties”. CRC Press, 2013. doi: 10.1201/9780429150999.

[30] E. S. Puchi-Cabrera, M. H. Staia, and A. Iost, “Modeling the composite hardness of multilayer coated systems,” *Thin Solid Films*, vol. 578, pp. 53–62, Mar. 2015, doi: 10.1016/j.tsf.2015.01.070.

[31] H. Nili, K. Kalantar-zadeh, M. Bhaskaran, and S. Sriram, “In situ nanoindentation: Probing nanoscale multifunctionality,” *Progress in Materials Science*, vol. 58, no. 1, pp. 1–29, Jan. 2013, doi: 10.1016/j.pmatsci.2012.08.001.

[32] J. S. Koehler, “Attempt to Design a Strong Solid,” *Phys. Rev. B*, vol. 2, no. 2, pp. 547–551, Jul. 1970, doi: 10.1103/PhysRevB.2.547.

[33] S. Veprek, M. G. J. Veprek-Heijman, P. Karvankova, and J. Prochazka, “Different approaches to superhard coatings and nanocomposites,” *Thin Solid Films*, vol. 476, no. 1, pp. 1–29, Apr. 2005, doi: 10.1016/j.tsf.2004.10.053.

[34] S. Sintonen, S. Ali, O. M. E. Ylivaara, R. L. Puurunen, and H. Lipsanen, “X-ray reflectivity characterization of atomic layer deposition Al_2O_3/TiO_2 nanolaminates with ultrathin bilayers,” *Journal of Vacuum Science & Technology A: Vacuum, Surfaces, and Films*, vol. 32, no. 1, p. 01A111, Jan. 2014, doi: 10.1116/1.4833556.

[35] Z. B. Qi, P. Sun, F. P. Zhu, Z. C. Wang, D. L. Peng, and C. H. Wu, “The inverse Hall–Petch effect in nanocrystalline ZrN coatings,” *Surface and Coatings Technology*, vol. 205, no. 12, pp. 3692–3697, Mar. 2011, doi: 10.1016/j.surfcoat.2011.01.021.

[36] R. L. Puurunen, “Surface chemistry of atomic layer deposition: A case study for the trimethylaluminum/water process,” *Journal of Applied Physics*, vol. 97, no. 12, p. 121301, Jun. 2005, doi: 10.1063/1.1940727.

[37] V. Miikkulainen, M. Leskelä, M. Ritala, and R. L. Puurunen, “Crystallinity of inorganic films grown by atomic layer deposition: Overview and general trends,” *Journal of Applied Physics*, vol. 113, no. 2, p. 021301, Jan. 2013, doi: 10.1063/1.4757907.

[38] G. Oya and Y. Sawada, “Molecular layer epitaxy of α-Al_2O_3 films,” *Journal of Crystal Growth*, vol. 99, no. 1, pp. 572–576, Jan. 1990, doi: 10.1016/0022-0248(90)90585-9.

[39] L. Aarik, H. Mändar, A. Tarre, H.-M. Piirsoo, and J. Aarik, “Mechanical properties of crystalline and amorphous aluminum oxide thin films grown by atomic layer deposition,” *Surface and Coatings Technology*, vol. 438, p. 128409, May 2022, doi: 10.1016/j.surfcoat.2022.128409.

[40] J. Aarik, A. Aidla, H. Mändar, T. Uustare, and V. Sammelselg, “Growth kinetics and structure formation of ZrO_2 thin films in chloride-based atomic layer deposition process,” *Thin Solid Films*, vol. 408, no. 1, pp. 97–103, Apr. 2002, doi: 10.1016/S0040-6090(02)00123-2.

[41] M. Nasim, “A review of high-strength nanolaminates and evaluation of their properties,” *Journal of Materials Science*, p. 30, 2020.

[42] S. M. George, “Atomic Layer Deposition: An Overview,” *Chem. Rev.*, vol. 110, no. 1, pp. 111–131, Jan. 2010, doi: 10.1021/cr900056b.

[43] W. J. H. Berghuis, J. Melskens, B. Macco, S. B. Basuvalingam, M. A. Verheijen, and W. M. M. Kessels, “Atomic layer deposition of Nb-doped TiO_2: Dopant incorporation and effect of annealing,” *Journal of Vacuum Science & Technology A: Vacuum, Surfaces, and Films*, vol. 38, no. 2, p. 022408, Mar. 2020, doi: 10.1116/1.5134743.

[44] P. Colombi, P. Zanola, E. Bontempi, R. Roberti, M. Gelfi, and L. E. Depero, “Glancing-incidence X-ray diffraction for depth profiling of polycrystalline layers,” *J Appl Crystallogr*, vol. 39, no. 2, pp. 176–179, Apr. 2006, doi: 10.1107/S0021889805042779.

[45] H. Mändar, J. Felsche, V. Mikli, and T. Vajakas, “*AXES* 1.9: new tools for estimation of crystallite size and shape by Williamson–Hall analysis,” *J Appl Crystallogr*, vol. 32, no. 2, pp. 345–350, Apr. 1999, doi: 10.1107/S0021889898011170.

[46] M. Lee, “X-Ray Diffraction for Materials Research: From Fundamentals to Applications” Apple Academic Press, 2016. doi: 10.1201/b19936

[47] I. Saito, T. Miyazaki, and K. Yamamoto, “Depth-Resolved Structure Analysis of Cylindrical Microdomain in Block Copolymer Thin Film by Grazing-Incidence Small-Angle X-ray Scattering Utilizing Low-Energy X-rays,” *Macromolecules*, vol. 48, no. 22, pp. 8190–8196, Nov. 2015, doi: 10.1021/acs.macromol.5b01883.

[48] L. G. Parratt, “Surface Studies of Solids by Total Reflection of X-Rays,” *Phys. Rev.*, vol. 95, no. 2, pp. 359–369, Jul. 1954, doi: 10.1103/PhysRev.95.359.

[49] G. Krautheim, T. Hecht, S. Jakschik, U. Schröder, and W. Zahn, “Mechanical stress in ALD-Al_2O_3 films,” *Applied Surface Science*, vol. 252, no. 1, pp. 200–204, Sep. 2005, doi: 10.1016/j.apsusc.2005.01.118.

[50] K. Kukli, M. Ritala, and M. Leskelä, “Atomic Layer Epitaxy Growth of Tantalum Oxide Thin Films from $Ta(OC_2H_5)_5$ and H_2O,” *J. Electrochem. Soc.*, vol. 142, no. 5, p. 1670, May 1995, doi: 10.1149/1.2048637.

[51] K. Kukli *et al.*, “Atomic layer deposition and properties of mixed Ta_2O_5 and ZrO_2 films,” *AIP Advances*, vol. 7, no. 2, p. 025001, Feb. 2017, doi: 10.1063/1.4975928.

[52] K. Yong Shin, P. SangHeeKo, Y. Sun Jin, and K. Jung Sook, “Effect of Rapid Thermal Annealing on the Structure and the Electrical Properties of Atomic-Layer-Deposited Ta_2O_5 Films,” *J. Korean Phys. Soc.*, vol. 37, no. 6, p. 975, Dec. 2000, doi: 10.3938/jkps.37.975.

[53] K.-H. Min, R. Sinclair, I.-S. Park, S.-T. Kim, and U.-I. Chung, “Crystallization behaviour of ALD-Ta_2O_5 thin films: the application of in-situ TEM,” *Philosophical Magazine*, vol. 85, no. 18, pp. 2049–2063, Jun. 2005, doi: 10.1080/14786430500036546.

[54] E. Çetinörgü-Goldenberg, J.-E. Klemberg-Sapieha, and L. Martinu, “Effect of postdeposition annealing on the structure, composition, and the mechanical and optical characteristics of niobium and tantalum oxide films,” *Appl. Opt., AO*, vol. 51, no. 27, pp. 6498–6507, Sep. 2012, doi: 10.1364/AO.51.006498.

[55] R. Hollerweger *et al.*, “Complementary ab initio and X-ray nanodiffraction studies of Ta_2O_5,” *Acta Materialia*, vol. 83, pp. 276–284, Jan. 2015, doi: 10.1016/j.actamat.2014.10.006.

[56] N. Song *et al.*, “Evaluation of Phase Transformation and Mechanical Properties of Metastable Yttria-Stabilized Zirconia by Nanoindentation,” *Materials*, vol. 12, no. 10, p. 1677, May 2019, doi: 10.3390/ma12101677.

[57] K. Koski, J. Hölsä, and P. Juliet, “Properties of zirconium oxide thin films deposited by pulsed reactive magnetron sputtering,” *Surface and Coatings Technology*, vol. 120–121, pp. 303–312, Nov. 1999, doi: 10.1016/S0257-8972(99)00501-0.

[58] K. Kalam, P. Ritslaid, T. Käämbre, A. Tamm, and K. Kukli, “Properties of tin oxide films grown by atomic layer deposition from tin tetraiodide and ozone,” *Beilstein J. Nanotechnol.*, vol. 14, pp. 1085–1092, Nov. 2023, doi: 10.3762/bjnano.14.89.

[59] T.-H. Fang and W.-J. Chang, “Nanomechanical characteristics of SnO_2:F thin films deposited by chemical vapor deposition,” *Applied Surface Science*, vol. 252, no. 5, pp. 1863–1869, Dec. 2005, doi: 10.1016/j.apsusc.2005.03.151.

[60] C. Lee, X. Wei, J. W. Kysar, and J. Hone, “Measurement of the Elastic Properties and Intrinsic Strength of Monolayer Graphene,” *Science*, vol. 321, no. 5887, pp. 385–388, Jul. 2008, doi: 10.1126/science.1157996.

[61] G.-H. Lee *et al.*, “High-Strength Chemical-Vapor–Deposited Graphene and Grain Boundaries,” *Science*, vol. 340, no. 6136, pp. 1073–1076, May 2013, doi: 10.1126/science.1235126.

[62] Z. D. Sha *et al.*, “On the failure load and mechanism of polycrystalline graphene by nanoindentation,” *Sci Rep*, vol. 4, no. 1, p. 7437, Dec. 2014, doi: 10.1038/srep07437.

[63] B. Larsen *et al.*, “Crystallization in Zirconia Film Nano-Layered with Silica,” *Nanomaterials*, vol. 11, no. 12, p. 3444, Dec. 2021, doi: 10.3390/nano11123444.

[64] D. Cao *et al.*, “Effects of rapid thermal annealing on the properties of HfO_2/La_2O_3 nanolaminate films deposited by plasma enhanced atomic layer deposition,” *Journal of Vacuum Science & Technology A*, vol. 33, no. 1, p. 01A116, Jan. 2015, doi: 10.1116/1.4900935.

[65] T. Arroval, L. Aarik, R. Rammula, V. Kruusla, and J. Aarik, “Effect of substrate-enhanced and inhibited growth on atomic layer deposition and properties of aluminum–titanium oxide films,” *Thin Solid Films*, vol. 600, pp. 119–125, Feb. 2016, doi: 10.1016/j.tsf.2016.01.024.

[66] A. C. Fischer-Cripps, *Nanoindentation*. in Mechanical Engineering Series. New York, NY: Springer New York, 2011. doi: 10.1007/978-1-4419-9872-9.

[67] Y. Wu *et al.*, “Dopant Distribution in Atomic Layer Deposited ZnO:Al Films Visualized by Transmission Electron Microscopy and Atom Probe Tomography,” *Chem Mater*, vol. 30, no. 4, pp. 1209–1217, Feb. 2018, doi: 10.1021/acs.chemmater.7b03501.

[68] G. P. Cousland, X. Y. Cui, A. E. Smith, A. P. J. Stampfl, and C. M. Stampfl, “Mechanical properties of zirconia, doped and undoped yttria-stabilized cubic zirconia from first-principles,” *Journal of Physics and Chemistry of Solids*, vol. 122, pp. 51–71, Nov. 2018, doi: 10.1016/j.jpcs.2018.06.003.

[69] G. Wang, F. Meng, C. Ding, P. K. Chu, and X. Liu, “Microstructure, bioactivity and osteoblast behavior of monoclinic zirconia coating with nanostructured surface,” *Acta Biomaterialia*, vol. 6, no. 3, pp. 990–1000, Mar. 2010, doi: 10.1016/j.actbio.2009.09.021.

[70] W. Weinreich *et al.*, “Structural properties of as deposited and annealed ZrO_2 influenced by atomic layer deposition, substrate, and doping,” *Journal of Vacuum Science & Technology A*, vol. 31, no. 1, p. 01A119, Nov. 2012, doi: 10.1116/1.4765047.

[71] C. Ricca, A. Ringuedé, M. Cassir, C. Adamo, and F. Labat, "A comprehensive DFT investigation of bulk and low-index surfaces of ZrO_2 polymorphs," *Journal of Computational Chemistry*, vol. 36, no. 1, pp. 9–21, 2015, doi: https://doi.org/10.1002/jcc.23761.

[72] M. Cassir, F. Goubin, C. Bernay, P. Vernoux, and D. Lincot, "Synthesis of ZrO_2 thin films by atomic layer deposition: growth kinetics, structural and electrical properties," *Applied Surface Science*, vol. 193, no. 1, pp. 120–128, Jun. 2002, doi: 10.1016/S0169-4332(02)00247-7.

[73] I. Kärkkänen *et al.*, "Study of atomic layer deposited ZrO_2 and ZrO_2/TiO_2 films for resistive switching application," *physica status solidi (a)*, vol. 211, no. 2, pp. 301–309, 2014, doi: 10.1002/pssa.201330034.

[74] D. M. Hausmann and R. G. Gordon, "Surface morphology and crystallinity control in the atomic layer deposition (ALD) of hafnium and zirconium oxide thin films," *Journal of Crystal Growth*, vol. 249, no. 1, pp. 251–261, Feb. 2003, doi: 10.1016/S0022-0248(02)02133-4.

[75] J. Aarik, A. Aidla, H. Mändar, V. Sammelselg, and T. Uustare, "Texture development in nanocrystalline hafnium dioxide thin films grown by atomic layer deposition," *Journal of Crystal Growth*, vol. 220, no. 1, pp. 105–113, Nov. 2000, doi: 10.1016/S0022-0248(00)00831-9.

[76] R. Wang *et al.*, "Interfacial and microstructural changes of the Al_2O_3/ZnO multilayer films induced by in-situ growth and post-annealing temperatures," *Materials Chemistry and Physics*, vol. 287, p. 126272, Aug. 2022, doi: 10.1016/j.matchemphys.2022.126272.

[77] P. Filippov and U. Koch, "Nanoindentation of Aluminum Single Crystals: Experimental Study on Influencing Factors," *Materials (Basel)*, vol. 12, no. 22, p. 3688, Nov. 2019, doi: 10.3390/ma12223688.

[78] O. B. Shcherbina, M. N. Palatnikov, and V. V. Efremov, "Mechanical properties of Nb_2O_5 and Ta_2O_5 prepared by different procedures," *Inorg Mater*, vol. 48, no. 4, pp. 433–438, Apr. 2012, doi: 10.1134/S0020168512040139.

ORIGINAL PUBLICATIONS

CURRICULUM VITAE

Name	Helle-Mai Piirsoo
Date of birth	24.12.1995
E-mail	helle-mai.piirsoo@ut.ee
ORCID	0000-0002-8246-7434

Education

2020–	University of Tartu, Doctor of Philosophy, Materials Science
2018–2020	University of Tartu, Master of Science, Materials Science (*cum laude*)
2015–2018	University of Tartu, Bachelor of Science, Materials Science (*cum laude*)
2012–2015	Nõo Secondary School of Science (*cum laude*)
2003–2012	Võnnu Secondary School

Work experience

2021–	University of Tartu, Institute of Physics, Junior Research Fellow in Materials Science
2019–2021	University of Tartu, Institute of Physics, Engineer
2016–2018	University of Tartu, Institute of Physics, Laboratory Assistant

Projects in progress

TT13 "Center of nanomaterials technologies and research (NAMUR+)" (1.01.2021−31.12.2024), Vambola Kisand, University of Tartu, Faculty of Science and Technology, Institute of Physics.

PRG753 "Resistive switching in artificially designed materials for data processing" (1.01.2020−31.12.2024), Kaupo Kukli, University of Tartu, Faculty of Science and Technology, Institute of Physics.

Publications

Ahmed, Z.; Akula, S.; Kozlova, J.; **Piirsoo, H.-M**.; Kukli, K.; Kikas, A.; Kisand, V.; Käärik, M.; Leis, J.; Treshchalov, A.; Aruväli, J.; Tammeveski, K. (2024). International Journal of Hydrogen Energy, 62, 849−858. DOI: 10.1016/j.ijhydene.2024.03.055.

Chambers, R.; **Piirsoo, H.-M**.; Tamm, A.; Kozlova, J.; Kukli, K.; Ritslaid, P.; Treshchalov, A.; Erikson, H.; Tammeveski, K. (2024). ACS Applied Nano Materials, 7 (6), 5943−5955. DOI: 10.1021/acsanm.3c05713.

Mooste, M.; Ahmed, Z.; Kapitulskis, P.; Ivanov, R.; Treshchalov, A.; **Piirsoo, H.-M**.; Kikas, A.; Kisand, V.; Kukli, K.; Hussainova, I.; Tammeveski, K. (2024). Applied Surface Science, 660, 160024. DOI: 10.1016/j.apsusc.2024.160024.

Yusibova, G.; Assafrei, J.-M.; Ping, K.; Aruväli, J.; Paiste, P.; Käärik, M.; Leis, J.; **Piirsoo, H.-M.**; Tamm, A.; Kikas, A.; Kisand, V.; Starkov, P.l; Kongi, N. (2023). Journal of Electroanalytical Chemistry, 930, 117161. DOI: 10.1016/j.jelechem.2023.117161.

Linge, J.M.; Erikson, H.; Mooste, M.; **Piirsoo, H.-M.**; Kaljuvee, T.; Kikas, A.; Aruväli, J.; Kisand, V.; Tamm, A.; Kannan, A.M.; Tammeveski, K. (2023). International Journal of Hydrogen Energy, 29, 11058−11070. DOI: 10.1016/j.ijhydene.2022.12.138.

Piirsoo, H.-M.; Jõgiaas, T.; Kukli, K.; Tamm, A. (2023). Materials, 16 (8), 3207. DOI: 10.3390/ma16083207.

Kull, M.; **Piirsoo, H.-M.**; Tarre, A.; Mändar, H.; Tamm, A.; Jõgiaas, T. (2023). Nanomaterials, 13 (10), 1607. DOI: 10.3390/nano13101607.

Lüsi, M.; Erikson, H.; **Piirsoo, H.-M**.; Aruväli, J.; Kikas, A.; Kisand, V.; Tamm, A.; Tammeveski, K. (2023). Applied Surface Science, 636, 157859. DOI: 10.1016/j.apsusc.2023.157859.

Muuli, K.; Kumar, R.; Mooste, M.; Gudkova, V.; Treshchalov, A.; **Piirsoo, H.-M.;** Kikas, A.; Aruväli, J.; Kisand, V.; Tamm, A.; Krumme, A.; Moni, P.; Wilhelm, M.; Tammeveski, K. (2023). Materials, 16 (13), 4626. DOI: 10.3390/ma16134626.

Akula, S.; Mooste, M.; Zulevi, B.; McKinney, S.; Kikas, A.; **Piirsoo, H.-M.;** Rahn, M.; Tamm, A.; Kisand, V.; Serov, A.; Creel, E.; Cullen, D.; Neyerlin, K.; Wang, H.; Odgaard, M.; Reshetenko, T.; Tammeveski, K. (2022). Journal of Power Sources, 520, ARTN 230819. DOI: 10.1016/j.jpowsour.2021.230819.

Kukli, K.; Lauri A.; Vinuesa, G.; Dueñas, S.; Castán, H.; García, H.; Kasikov, A.; Ritslaid, P.; **Piirsoo, H.-M.**; Aarik, J. (2022). Materials, 15 (3), 877. DOI: 10.3390/ma15030877.

Merisalu, M.; Aarik, L.; Kozlova, J.; Mandar, H.; Tarre, A**.; Piirsoo, H-M**.; Sammelselg, V. (2022). Surface and Coatings Technology, 435, 128240. DOI: 10.1016/j.surfcoat.2022.128240.

Tamm, A.; Kahro, T.; **Piirsoo, H.-M.**; Jõgiaas, T. (2022). Applied Sciences, 12 (5), 2491. DOI: 10.3390/app12052491.

Piirsoo, H.-M.; Jõgiaas, T.; Ritslaid, P.; Kukli, K.; Tamm, A. (2022). Coatings, 12 (3), 404. DOI: 10.3390/coatings12030404.

Aarik, L.; Mändar, H.; Tarre, A.; **Piirsoo, H.-M.**; Aarik, J. (2022). Surface and Coatings Technology, 438. DOI: 10.1016/j.surfcoat.2022.128409.

Lüsi, M.; Erikson, H.; **Piirsoo, H.-M.**; Paiste, P.; Aruväli, J.; Kikas, A.; Kisand, V.; Tamm, A.; Tammeveski, K. (2022). Journal of Electroanalytical Chemistry, 917, 116391. DOI: 10.1016/j.jelechem.2022.116391.

Veske, K.; Sarapuu, A.; Käärik, M.; Kikas, A.; Kisand, V.; **Piirsoo, H.-M**.; Treshchalov, A.; Leis, J.; Tamm, A.; Tammeveski, K. (2022). Catalysts, 12 (5), 568. DOI: 10.3390/catal12050568.

Abelniece, Z.; Kampars, V.; **Piirsoo, H.-M.**; Mändar, H.; Tamm, A. (2022). Environmental Progress & Sustainable Energy, e13905. DOI: 10.1002/ep.13905.

Abelniece, Z.; Kampars, V.; **Piirsoo, H.-M.**; Mändar, H.; Tamm, A. (2022). Energy Reports, 8 (S16), 625−629. DOI: 10.1016/j.egyr.2022.10.319.

Kisand, K.; Sarapuu, A.; Douglin, J.C.; Kikas, A.; Treshchalov, A.; Käärik, M.; **Piirsoo, H.-M**.; Paiste, P.; Aruväli, J.; Leis, J.; Kisand, V.; Tamm, A.; Dekel, D.R.; Tammeveski, K (2022). ACS Catalysis, 12 (22), 14050−14061. DOI: 10.1021/acscatal.2c03683.

Merisalu, M.; Aarik, L.**; Piirsoo, H.-M.**; Kozlova, J.; Tarre, A.; Zabels, R.; Wessing, J.; Brieva, A.; Sammelselg, V. (2022). Journal of The Electrochemical Society, 169 (7), ARTN 071503. DOI: 10.1149/1945-7111/ac7bb2.

Abelniece, Z.; **Piirsoo, H.-M.**; Mändar, H.; Tamm, A. (2022). 22nd SGEM International Multidisciplinary Scientific GeoConference Proceedings 2022, Energy and Clean Technologies, 4.1. STEF92 Technology, 13−18. DOI: 10.5593/sgem2022/4.1/s17.02.

Kisand, K.; Sarapuu, A.; Kikas, A.; Kisand, V.; Rähn, M.; Treshchalov, A.; Käärik, M.; **Piirsoo, H.-M**.; Aruväli, J.; Paiste, P.; Leis, J.; Sammelselg, V.; Tamm, A.; Tammeveski, K. (2021). Electrochemistry Communications, 124, ARTN 106932. DOI: 10.1016/j.elecom.2021.106932.

Lilloja, J.; Mooste, M.; Kibena-Põldsepp, E.; Sarapuu, A.; Zulevi, B.; Kikas, A.; **Piirsoo, H.-M**.; Tamm, A.; Kisand, V.; Holdcroft, S.; Serov, A.; Tammeveski, K. (2021). Journal of Power Sources Advances, 8, 100052. DOI: 10.1016/j.powera.2021.100052.

Piirsoo, H.-M.; Jõgiaas, T.; Mändar, H.; Ritslaid, P.; Kukli, K.; Tamm, A. (2021). AIP Advances, 11 (5), 055316. DOI: 10.1063/5.0047572.

Abelniece, Z.; Kampars, V.; **Piirsoo, H.-M.**; Tamm, A. (2021) E3S Web of Conferences, 259, 04001. DOI: 10.1051/e3sconf/202125904001.

Kahro, T.; Tarre, A.; Käämbre, T.; **Piirsoo, H.-M.**; Kozlova, J.; Ritslaid, P.; Kasikov, A.; Jõgiaas, T.; Vinuesa, G.; Dueñas, S.; Castán, H.; Tamm, A.; Kukli, K. (2021). ACS Applied Nano Materials, 4 (5), 5152−5163. DOI: 10.1021/acsanm.1c00587.

Jõgi, I; Paris, P; Piip, K; Ristkok, J; Talviste, R; **Piirsoo, H-M**; Tamm, A; Grigore, E; Hakola, A; Tyburska-Pueschel, B; van der Meiden, H J (2021). Physica Scripta, 96 (11), 114010. DOI: 10.1088/1402-4896/ac169c.

Lüsi, M.; Erikson, H.; Tammeveski, K.; Treshchalov, A.; Kikas, A.; **Piirsoo, H.-M**.; Kisand, V.; Tamm, A.; Aruväli, J.; Solla-Gullón, J.; Feliu, J.M. (2021). Electrochimica Acta, 394, 139132. DOI: 10.1016/j.electacta.2021.139132.

Tamm, A.; **Piirsoo, H.-M.**; Jõgiaas, T.; Tarre, A.; Link, J.; Stern, R.; Kukli, K. (2021). Nanomaterials, 11 (7), ARTN 1633. DOI: 10.3390/nano11071633.

Abelniece, Z.; Kampars, V.; **Piirsoo, H.M**.; Mändar, H.; Tamm, A. (2021). International Multidisciplinary Scientific GeoConference Surveying Geology and Mining Ecology Management, SGEM, 21. Elsiver, 119−126. DOI: 10.5593/sgem2021/4.1/s17.23.

Kahro, T.; Castán, H.; Dueñas, S.; Merisalu, J.; Kozlova, J.; Jõgiaas, T.; **Piirsoo, H.-M.**; Kasikov, A.; Ritslaid, P.; Mändar, H.; Tarre, A.; Tamm, A.; Kukli, K. (2020). Journal of Vacuum Science & Technology A: Vacuum Surfaces and Films, 38 (6), 063411. DOI: 10.1116/6.0000390.

Conference Poster Presentations

Piirsoo, H.-M.; Jõgiaas, T.; Rad, Z.J.; Miettinen, M.; Laukkanen, P.; Kukli, K.; Tamm, A. Mechanical Behavior upon Annealing-induced Blistering of Atomic Layer Deposited Alumina Thin Film Layered with Tantala. EuroCVD/ Baltic ALD 2023, Leuven, Belgia, 29th May-2nd June.

Piirsoo, H.-M.; Jõgiaas, T.; Rad, Z.J.; Miettinen, M.; Laukkanen, P.; Kukil, K.; Tamm, A. Mechanical behavior of atomic layer deposited alumina-tantala thin films after annealing-induced blistering. GSFMT Scientific Conference 2023, Tartu, 23rd–24th May.

Piirsoo, H.-M.; Jõgiaas, T.; Ritslaid, P.; Kukli, K.; Tamm, A. Influence to Hardness of Alternating Sequence of Atomic Layer Deposited Harder Alumina and Softer Tantala Nanolaminates. GSFMT Scientific Conference 2022, Tallinn, 17th–18th May.

Piirsoo, H.-M.; Jõgiaas, T.; Ritslaid, P.; Kukli, K.; Tamm, A. Influence to Hardness of Alternating Sequence of Atomic Layer Deposited Harder Alumina and Softer Tantala Nanolaminates. ALD 2022, 22nd International Conference on Atomic Layer Deposition, Gent, Belgia, 26th–29th June.

Piirsoo, H.-M.; Jõgiaas, T.; Mändar, H.; Ritslaid, P.; Kukli, K.; Tamm, A. Microstructure and mechanical properties of atomic layer deposited alumina doped zirconia. GSFMT Scientific Conference 2021, Tartu, 14th–15th June.

ELULOOKIRJELDUS

Nimi Helle-Mai Piirsoo
Sünniaeg 24.12.1995
E-post helle-mai.piirsoo@ut.ee
ORCID 0000-0002-8246-7434

Hariduskäik

2020–	Tartu Ülikool, doktoriõpe, materjaliteadus
2018–2020	Tartu Ülikool, magistriõpe, materjaliteadus (*cum laude*)
2015–2018	Tartu Ülikool, bakalaureuseõpe, materjaliteadus (*cum laude*)
2012–2015	Nõo Reaalgümnaasium (kuldmedal)
2003–2012	Võnnu Keskkool

Töökohad ja ametid

2021–	Tartu Ülikool, füüsika instituut, materjaliteaduse nooremteadur
2019–2021	Tartu Ülikool, füüsika instituut, insener
2016–2018	Tartu Ülikool, füüsika instituut, laborant

Jooksvad projektid

TT13 "Nanomaterjalide tehnoloogiate ja uuringute keskus (NAMUR+)" (1.01.2021−31.12.2024), Vambola Kisand, Tartu Ülikool, Loodus- ja täppisteaduste valdkond, füüsika instituut.

PRG753 "Takistuslülitusnähtused andmetöötluseks loodud tehismaterjalides" (1.01.2020−31.12.2024), Kaupo Kukli, Tartu Ülikool, Loodus- ja täppisteaduste valdkond, füüsika instituut.

Publikatsioonid

Ahmed, Z.; Akula, S.; Kozlova, J.; **Piirsoo, H.-M**.; Kukli, K.; Kikas, A.; Kisand, V.; Käärik, M.; Leis, J.; Treshchalov, A.; Aruväli, J.; Tammeveski, K. (2024). International Journal of Hydrogen Energy, 62, 849−858. DOI: 10.1016/j.ijhydene.2024.03.055.

Chambers, R.; **Piirsoo, H.-M**.; Tamm, A.; Kozlova, J.; Kukli, K.; Ritslaid, P.; Treshchalov, A.; Erikson, H.; Tammeveski, K. (2024). ACS Applied Nano Materials, 7 (6), 5943−5955. DOI: 10.1021/acsanm.3c05713.

Mooste, M.; Ahmed, Z.; Kapitulskis, P.; Ivanov, R.; Treshchalov, A.; **Piirsoo, H.-M**.; Kikas, A.; Kisand, V.; Kukli, K.; Hussainova, I.; Tammeveski, K. (2024). Applied Surface Science, 660, 160024. DOI: 10.1016/j.apsusc.2024.160024.

Yusibova, G.; Assafrei, J.-M.; Ping, K.; Aruväli, J.; Paiste, P.; Käärik, M.; Leis, J.; **Piirsoo, H.-M.**; Tamm, A.; Kikas, A.; Kisand, V.; Starkov, P.l; Kongi, N. (2023). Journal of Electroanalytical Chemistry, 930, 117161. DOI: 10.1016/j.jelechem.2023.117161.

Linge, J.M.; Erikson, H.; Mooste, M.; **Piirsoo, H.-M.**; Kaljuvee, T.; Kikas, A.; Aruväli, J.; Kisand, V.; Tamm, A.; Kannan, A.M.; Tammeveski, K. (2023). International Journal of Hydrogen Energy, 29, 11058−11070. DOI: 10.1016/ j.ijhydene.2022.12.138.

Piirsoo, H.-M.; Jõgiaas, T.; Kukli, K.; Tamm, A. (2023). Materials, 16 (8), 3207. DOI: 10.3390/ma16083207.

Kull, M.; **Piirsoo, H.-M.**; Tarre, A.; Mändar, H.; Tamm, A.; Jõgiaas, T. (2023). Nanomaterials, 13 (10), 1607. DOI: 10.3390/nano13101607.

Lüsi, M.; Erikson, H.; **Piirsoo, H.-M**.; Aruväli, J.; Kikas, A.; Kisand, V.; Tamm, A.; Tammeveski, K. (2023). Applied Surface Science, 636, 157859. DOI: 10.1016/j.apsusc.2023.157859.

Muuli, K.; Kumar, R.; Mooste, M.; Gudkova, V.; Treshchalov, A.; **Piirsoo, H.-M.;** Kikas, A.; Aruväli, J.; Kisand, V.; Tamm, A.; Krumme, A.; Moni, P.; Wilhelm, M.; Tammeveski, K. (2023). Materials, 16 (13), 4626. DOI: 10.3390/ma16134626.

Akula, S.; Mooste, M.; Zulevi, B.; McKinney, S.; Kikas, A.; **Piirsoo, H.-M.;** Rahn, M.; Tamm, A.; Kisand, V.; Serov, A.; Creel, E.; Cullen, D.; Neyerlin, K.; Wang, H.; Odgaard, M.; Reshetenko, T.; Tammeveski, K. (2022). Journal of Power Sources, 520, ARTN 230819. DOI: 10.1016/j.jpowsour.2021.230819.

Kukli, K.; Lauri A.; Vinuesa, G.; Dueñas, S.; Castán, H.; García, H.; Kasikov, A.; Ritslaid, P.; **Piirsoo, H.-M.**; Aarik, J. (2022). Materials, 15 (3), 877. DOI: 10.3390/ma15030877.

Merisalu, M.; Aarik, L.; Kozlova, J.; Mandar, H.; Tarre, A**.; Piirsoo, H-M**.; Sammelselg, V. (2022). Surface and Coatings Technology, 435, 128240. DOI: 10.1016/j.surfcoat.2022.128240.

Tamm, A.; Kahro, T.; **Piirsoo, H.-M.**; Jõgiaas, T. (2022). Applied Sciences, 12 (5), 2491. DOI: 10.3390/app12052491.

Piirsoo, H.-M.; Jõgiaas, T.; Ritslaid, P.; Kukli, K.; Tamm, A. (2022). Coatings, 12 (3), 404. DOI: 10.3390/coatings12030404.

Aarik, L.; Mändar, H.; Tarre, A.; **Piirsoo, H.-M.**; Aarik, J. (2022). Surface and Coatings Technology, 438. DOI: 10.1016/j.surfcoat.2022.128409.

Lüsi, M.; Erikson, H.; **Piirsoo, H.-M.**; Paiste, P.; Aruväli, J.; Kikas, A.; Kisand, V.; Tamm, A.; Tammeveski, K. (2022). Journal of Electroanalytical Chemistry, 917, 116391. DOI: 10.1016/j.jelechem.2022.116391.

Veske, K.; Sarapuu, A.; Käärik, M.; Kikas, A.; Kisand, V.; **Piirsoo, H.-M**.; Treshchalov, A.; Leis, J.; Tamm, A.; Tammeveski, K. (2022). Catalysts, 12 (5), 568. DOI: 10.3390/catal12050568.

Abelniece, Z.; Kampars, V.; **Piirsoo, H.-M.**; Mändar, H.; Tamm, A. (2022). Environmental Progress & Sustainable Energy, e13905. DOI: 10.1002/ ep.13905.

Abelniece, Z.; Kampars, V.; **Piirsoo, H.-M.**; Mändar, H.; Tamm, A. (2022). Energy Reports, 8 (S16), 625−629. DOI: 10.1016/j.egyr.2022.10.319.

Kisand, K.; Sarapuu, A.; Douglin, J.C.; Kikas, A.; Treshchalov, A.; Käärik, M.; **Piirsoo, H.-M**.; Paiste, P.; Aruväli, J.; Leis, J.; Kisand, V.; Tamm, A.; Dekel, D.R.; Tammeveski, K (2022). ACS Catalysis, 12 (22), 14050−14061. DOI: 10.1021/acscatal.2c03683.

Merisalu, M.; Aarik, L.**; Piirsoo, H.-M.**; Kozlova, J.; Tarre, A.; Zabels, R.; Wessing, J.; Brieva, A.; Sammelselg, V. (2022). Journal of The Electrochemical Society, 169 (7), ARTN 071503. DOI: 10.1149/1945-7111/ac7bb2.

Abelniece, Z.; **Piirsoo, H.-M.**; Mändar, H.; Tamm, A. (2022). 22nd SGEM International Multidisciplinary Scientific GeoConference Proceedings 2022, Energy and Clean Technologies, 4.1. STEF92 Technology, 13−18. DOI: 10.5593/sgem2022/4.1/s17.02.

Kisand, K.; Sarapuu, A.; Kikas, A.; Kisand, V.; Rähn, M.; Treshchalov, A.; Käärik, M.; **Piirsoo, H.-M**.; Aruväli, J.; Paiste, P.; Leis, J.; Sammelselg, V.; Tamm, A.; Tammeveski, K. (2021). Electrochemistry Communications, 124, ARTN 106932. DOI: 10.1016/j.elecom.2021.106932.

Lilloja, J.; Mooste, M.; Kibena-Põldsepp, E.; Sarapuu, A.; Zulevi, B.; Kikas, A.; **Piirsoo, H.-M**.; Tamm, A.; Kisand, V.; Holdcroft, S.; Serov, A.; Tammeveski, K. (2021). Journal of Power Sources Advances, 8, 100052. DOI: 10.1016/j.powera.2021.100052.

Piirsoo, H.-M.; Jõgiaas, T.; Mändar, H.; Ritslaid, P.; Kukli, K.; Tamm, A. (2021). AIP Advances, 11 (5), 055316. DOI: 10.1063/5.0047572.

Abelniece, Z.; Kampars, V.; **Piirsoo, H.-M.**; Tamm, A. (2021) E3S Web of Conferences, 259, 04001. DOI: 10.1051/e3sconf/202125904001.

Kahro, T.; Tarre, A.; Käämbre, T.; **Piirsoo, H.-M.**; Kozlova, J.; Ritslaid, P.; Kasikov, A.; Jõgiaas, T.; Vinuesa, G.; Dueñas, S.; Castán, H.; Tamm, A.; Kukli, K. (2021). ACS Applied Nano Materials, 4 (5), 5152−5163. DOI: 10.1021/acsanm.1c00587.

Jõgi, I; Paris, P; Piip, K; Ristkok, J; Talviste, R; **Piirsoo, H-M**; Tamm, A; Grigore, E; Hakola, A; Tyburska-Pueschel, B; van der Meiden, H J (2021). Physica Scripta, 96 (11), 114010. DOI: 10.1088/1402-4896/ac169c.

Lüsi, M.; Erikson, H.; Tammeveski, K.; Treshchalov, A.; Kikas, A.; **Piirsoo, H.-M**.; Kisand, V.; Tamm, A.; Aruväli, J.; Solla-Gullón, J.; Feliu, J.M. (2021). Electrochimica Acta, 394, 139132. DOI: 10.1016/j.electacta.2021.139132.

Tamm, A.; **Piirsoo, H.-M.**; Jõgiaas, T.; Tarre, A.; Link, J.; Stern, R.; Kukli, K. (2021). Nanomaterials, 11 (7), ARTN 1633. DOI: 10.3390/nano11071633.

Abelniece, Z.; Kampars, V.; **Piirsoo, H.M**.; Mändar, H.; Tamm, A. (2021). International Multidisciplinary Scientific GeoConference Surveying Geology and Mining Ecology Management, SGEM, 21. Elsiver, 119−126. DOI: 10.5593/sgem2021/4.1/s17.23.

Kahro, T.; Castán, H.; Dueñas, S.; Merisalu, J.; Kozlova, J.; Jõgiaas, T.; **Piirsoo, H.-M.**; Kasikov, A.; Ritslaid, P.; Mändar, H.; Tarre, A.; Tamm, A.; Kukli, K. (2020). Journal of Vacuum Science & Technology A: Vacuum Surfaces and Films, 38 (6), 063411. DOI: 10.1116/6.0000390.

Konverentsi stendiettekanded

Piirsoo, H.-M.; Jõgiaas, T.; Rad, Z.J.; Miettinen, M.; Laukkanen, P.; Kukli, K.; Tamm, A. Mechanical Behavior upon Annealing-induced Blistering of Atomic Layer Deposited Alumina Thin Film Layered with Tantala. EuroCVD/ Baltic ALD 2023, Leuven, Belgia, 29. mai–2. juuni.

Piirsoo, H.-M.; Jõgiaas, T.; Rad, Z.J.; Miettinen, M.; Laukkanen, P.; Kukil, K.; Tamm, A. Mechanical behavior of atomic layer deposited alumina-tantala thin films after annealing-induced blistering. GSFMT Scientific Conference 2023, Tartu, 23.–24.mai.

Piirsoo, H.-M.; Jõgiaas, T.; Ritslaid, P.; Kukli, K.; Tamm, A. Influence to Hardness of Alternating Sequence of Atomic Layer Deposited Harder Alumina and Softer Tantala Nanolaminates. GSFMT Scientific Conference 2022, Tallinn, 17.–18.mai.

Piirsoo, H.-M.; Jõgiaas, T.; Ritslaid, P.; Kukli, K.; Tamm, A. Influence to Hardness of Alternating Sequence of Atomic Layer Deposited Harder Alumina and Softer Tantala Nanolaminates. ALD 2022, 22nd International Conference on Atomic Layer Deposition, Gent, Belgia, 26.–29.juuni.

Piirsoo, H.-M.; Jõgiaas, T.; Mändar, H.; Ritslaid, P.; Kukli, K.; Tamm, A. Microstructure and mechanical properties of atomic layer deposited alumina doped zirconia. GSFMT Scientific Conference 2021, Tartu, 14.–15.juuni.

DISSERTATIONES SCIENTIAE MATERIALIS UNIVERSITATIS TARTUENSIS

1. **Martin Järvekülg**. Tubular microstructures by Hf-, Zr- and Ti-butoxide gel sheet rolling. Tartu, 2011, 112 p.
2. **Sergei Vlassov.** Investigation of nanoscale interactions and mechanical properties of nanostructures using quartz tuning fork based real-time measurements. Tartu, 2011, 171 p.
3. **Margus Kodu**. Pulsed Laser Deposition of Magnesium Oxide and Barium Ternary Oxides for Plasma Display Protective Layers. Tartu, 2011, 89 p.
4. **Rainer Pärna**. Surface studies of some oxide films. Tartu, 2011, 129 p.
5. **Jevgeni Šulga**. Self-assembly and interaction of nanostructures. Tartu, 2011, 114 p.
6. **Wojciech Kuznik**. Quantum-chemical computer simulations of the linear and non-linear optical properties of pyrazoloquinoline and dicyanopyrazine derivatives. Tartu, 2012, 89 p.
7. **Leonid Dorogin**. Structural and tribological properties of zero- and one-dimensional nanocrystals. Tartu, 2012, 193 p.
8. **Viljar Palmre**. Fabrication and characterization of microporous carbon-based electroactive polymer actuators. Tartu, 2012, 99 p.
9. **Madis Paalo**. Synthesis of CNT-metal oxide nanocomposites: sol-gel process, rheology, structural and functional properties. Tartu, 2014, 175 p.
10. **Raul Välbe**. Developement of ionic liquid composites by sol-gel method for elaboration of industrial nano- and microstructures. Tartu, 2014, 97 p.
11. **Urmas Joost**. Impurity and preparation dependent properties of titania thin films. Tartu, 2014, 155 p.
12. **Madis Umalas**. Application of sol-gel technology for production of ceramic nanocomposites and functional coatings. Tartu, 2015, 136 p.
13. **Elena Samsonova**. Energy transfer probe as a tool to study morphological and structural origins of fluorescence quenching in rare-earth doped nanophosphors. Tartu, 2015, 114 p.
14. **Jay Mondal**. Novel Corrosion Protective Nanostructured Composite Coatings. Tartu, 2016, 104 p.
15. **Kathriin Utt**. Metal oxide mesostructures for optical applications. Tartu, 2016, 88 p.
16. **Kaido Siimon**. Electrospun gelatin cross-linked by glucose. Tartu, 2016, 84 p.
17. **Marko Part**. Combined three-dimensional sol-gel structures and atomic layer deposited thin films. Tartu, 2017, 162 p.
18. **Pejman Rasti**. Analysis of Remote Sensing Image Super Resolution using Fluid Lenses. Tartu, 2017, 188 p.
19. **Ivo Romet**. Recombination luminescence of doped borates: origin and application prospects in dosimetry. Tartu, 2017, 111 p.

20. **Vladimir I. Kondratiev**. Processing and characterization of transparent electrode materials. Tartu, 2017, 111 p.
21. **Taivo Jõgiaas**. Mechanical properties of atomic layer deposited thin films and nanocomposites. Tartu, 2017, 125 p.
22. **Lauri Aarik**. Atomic layer deposition and characterization of thin oxide films for application in protective coatings. Tartu, 2017, 180 p.
23. **Triin Kangur**. Preparation and functional properties of stochastic micro-structured sol-gel silica materials. Tartu, 2018, 96 p.
24. **Marta Berholts**. Fragmentation of ionic and hydrogen-bonded molecules induced by synchrotron radiation. Tartu, 2018, 126 p.
25. **Priit Priimägi**. Development and optimization of 3D-microbatteries. Tartu, 2018, 118 p.
26. **Siim Hödemann**. Residual stress determination in chemically strengthened and thermally tempered glass plates using scattered light method. Tartu, 2019, 146 p.
27. **Jekaterina Kozlova**. Complex characterization of graphene structures on nanometer level. Tartu, 2019, 206 p.
28. **Kristjan Kalam**. Magnetic, electric and structural properties of atomic layer deposited zirconia-based nanolaminates and mixtures. Tartu, 2020, 94 p.
29. **Triinu Vihmann**. Ionic liquids: synthesis and application in lubrication and lithography. Tartu, 2020, 102 p.
30. **Helina Seemen**. Atomic layer deposition and microscopic analysis of magnetically and electrically polarizable thin solid films. Tartu, 2021, 126 p.
31. **Ekaterina Vagapova**. Fluorescence quenching in inorganic crystalline solids activated by neodymium ions; from bulk to micro- and nanocrystals. Tartu, 2021, 116 p.
32. **Evgenii Strugovshchikov**. First-principles studies on rare-earth metal-hydride-based smart materials. Tartu, 2021, 166 p.
33. **Maido Merisalu**. Nanostructured Coatings for Car and Aerospace Industries. Tartu, 2022, 179 p.
34. **Elena Vinogradova**. Optical centers and quantum entangled states of Nd3+ ions in doped fluoride crystals. Tartu, 2023, 92 p.
35. **Dmytro Danilian**. “Photocatalytic materials for water treatment and antimicrobial applications”. Tartu, 2024, 139 p.
36. **Kristel Möls**. Metastable TiO_2-II in atomic layer deposited thin and ultrathin films: stabilization, properties and impact on film growth. Tartu, 2024, 112 p.